

Cirrus-induced shortwave radiative effects depending on their optical and physical properties: Case studies using simulations and measurements

5 Carmen Córdoba-Jabonero^{a,1,*}, Laura Gómez-Martín^{a,*}, Ana del Águila^{b,2}, José Manuel Vilaplana^b,
María-Ángeles López-Cayuela^a and María-Paz Zorzano^{c,d}

^aInstituto Nacional de Técnica Aeroespacial (INTA), Atmospheric Research and Instrumentation Branch, Torrejón de Ardoz, 28850-Madrid, Spain

10 ^bInstituto Nacional de Técnica Aeroespacial (INTA), Atmospheric Research and Instrumentation Branch, Atmospheric Sounding Station “El Arenosillo”, 21130-Huelva, Spain

^cCentro de Astrobiología (CSIC-INTA), Ctra. Ajalvir, km. 4, Torrejón de Ardoz, 28850-Madrid, Spain

^dDepartment of Computer Science, Electrical and Space Engineering, Luleå University of Technology, Luleå, Sweden

15 ¹Corresponding author: Carmen Córdoba-Jabonero, cordobajc@inta.es, Instituto Nacional de Técnica Aeroespacial (INTA), Atmospheric Research and Instrumentation Branch, Ctra. Ajalvir, km. 4, Torrejón de Ardoz, 28850-Madrid, Spain

²Present address: Remote Sensing Technology Institute, German Aerospace Center (DLR), 82234-Oberpfaffenhofen, Germany

20 *Equally contributing.

ABSTRACT

25 Cirrus (Ci) clouds play an important role in the atmospheric radiative balance, and hence in Climate Change. In this work, a polarized Micro-Pulse Lidar (P-MPL), standard NASA/Micro Pulse NETwork (MPLNET) system, deployed at the INTA/El Arenosillo station in Huelva (SW Iberian Peninsula) is used for Ci detection and characterization for the first time at this site. Three days were selected on the basis of the predominantly detected Ci clouds in dependence on their cloud optical depth (COD). Hence, three Ci cloud categories were examined at day-times for comparison with solar radiation issues: 19 cases of sub-visually (svCi, COD: 0.01-0.03) on 1 October 2016, 7 cases of semitransparents (stCi, COD: 0.03-0.30) on 8 May 2017, and 17 cases of opaques (opCi, COD: 0.3-3.0) on 28 October 2016. Their radiative-relevant optical, macro- and micro-physical properties were retrieved. The mean COD for the svCi, stCi and opCi groups was 0.02 ± 0.01 , 0.22 ± 0.08 and 0.93 ± 0.40 , respectively; in overall, their lidar ratio ranged between 25 and 35 sr. Ci clouds were detected at 11-13 km height (top boundaries) with geometrical thicknesses of 1.7-2.0 km. Temperatures reported at those altitudes corresponded to lower values than the thermal threshold for homogenous ice formation. Volume linear depolarization ratios of 0.3-0.4 (and normalized backscattering ratios higher than 0.9) also confirmed Ci clouds purely composed of ice particles. Their effective radius was within the interval of 9-15 μm size, and the ice water path ranged from 0.02 (svCi) to 9.9 (opCi) g m^{-2} . The Cirrus Cloud Radiative Effect (CCRE) was estimated using a RT model for Ci-free conditions and Ci-mode (Ci presence) scenarios. RT simulations were performed for deriving the CCRE at the top-of atmosphere (TOA) and on surface (SRF), and also the atmospheric CCRE, for the overall shortwave (SW) range and their spectral sub-intervals (UV, VIS and NIR). A good agreement was first obtained for the RT simulations as validated against solar radiation measurements under clean conditions for solar zenith angles less than 75°

45

(differences were mainly within $\pm 20 \text{ W m}^{-2}$ and correlation coefficients close to 1). By considering all the Ci clouds, independently on their COD, the mean SW CCRE values at TOA and SRF were, respectively, -30 ± 26 and $-24 \pm 19 \text{ W m}^{-2}$, being the mean atmospheric CCRE of $-7 \pm 7 \text{ W m}^{-2}$; these values are in good agreement with global annual estimates found for Ci clouds. By using linear regression analysis, a Ci-induced enhancing cooling radiative effect was observed as COD increased for all the spectral ranges, with high correlations. In particular, the SW CCRE at TOA and SRF, and the atmospheric CCRE, presented COD-dependent rates of -74 ± 4 , -55 ± 5 , $-19 \pm 2 \text{ W m}^{-2} \tau^{-1}$, respectively. Additionally, increasing negative rates are found from UV to NIR for each Ci category, reflecting a higher cooling NIR contribution w.r.t. UV and VIS ranges to the SW CCRE, and being also more pronounced at the TOA w.r.t. on SRF, as expected. The contribution of the SW CCRE to the net (SW+LW) radiative balance can be also potentially relevant. Results are especially significant for space-borne photometric/radiometric instrumentation and can contribute to validation purposes of the next ESA's EarthCARE mission, whose principal scientific goal is focused on radiation-aerosol-cloud interaction research.

60

Keywords: Cirrus Clouds, Cloud Optical Depth, Ice Water Path; Micro-Pulse Lidar, Shortwave radiative effects.

65

1. INTRODUCTION

70 Cirrus (Ci) clouds play an important role in the radiative balance of the atmosphere, and then in Climate Change research (Myhre et al., 2013; IPCC, 2013). The degree of understanding of the Cirrus-induced climatological implications is still low. Cirrus features are widely required in data assimilation for global/regional climatic models and satellite validation. In particular, the contribution of Ci-contrails formed from air traffic contamination is also poorly known. In addition, Ci cloud properties, both macrophysical and optical, affect the solar radiation levels reaching the ground, enhancing or decreasing the global warming effect (Boucher et al., 2013).
75 Thereby, a better understanding of Ci cloud properties is needed in order to explain their influence in the atmospheric radiative balance.

80 Ci clouds are the most common clouds in the atmosphere (e.g., Stubenrauch et al., 2013, and references therein). Numerous studies have been carried out with an especial emphasis in determining their optical and macrophysical properties related to seasonal effects, latitudinal diversity and climate implications (i.e., Keckhut et al., 2005; Dupont and Haeffelin, 2008; Garret, 2008; Dupont et al., 2010; Barja and Antuña, 2011; Campbell et al., 2015, 2016; Kienast-Sjögren et al., 2016; Córdoba-Jabonero et al., 2017). Those works show an increasing interest in Ci cloud-radiation interaction research. In this framework, relatively recent studies were focused on comparing two radiative transfer models for studying the radiative impact of single-layer cirrus clouds (Lolli et al., 2017a), highlighting those two models could provide significantly different radiative results. In addition, the effects of Ci clouds in radiative forcing have revealed different implications depending on the surface, land or water (Lolli et al., 2017b). However, the degree of knowledge about Ci cloud-radiation interactions is still low.

90 Cirrus clouds are the highest ice clouds formed in the troposphere, ranging from 7 km up to the tropopause. Ci top heights are usually located at altitudes corresponding to temperatures lower than the thermal ice formation threshold in homogenous processes, which is stated at either -37°C (Campbell et al., 2016) or -38°C (Krämer et al., 2016). The homogenous mechanisms that lead to form Ci clouds may vary with weather conditions (Krämer et al., 2016). Ice crystals contained in Ci clouds present different features, regarding their particle size, phase and orientation, in terms of their Ice Water Content (IWC; or Ice Water Path, IWP). A relationship is clearly observed between the Cloud Optical Depth (COD) and the IWC (i.e., Fu, 1996; Heymsfield et al., 2014; Kuhn and Heymsfield, 2016). Cirrus clouds are generally optically thinner, with low COD and low IWC, than the so-called 'warmer' Cirrus (containing a low proportion of liquid water content), which are optically thicker (high COD and high IWC). Hence, the radiative effects of the Ci clouds in dependence of their COD might differ.
100

105 It is generally believed that Ci clouds create a cooling effect, because they reflect incoming solar radiation. However, at the same time, these clouds can have a greenhouse effect because they absorb the infrared radiation from the Earth and as they are located at high altitudes with low temperatures, they emit little infrared radiation. The net effect depends on their COD, their altitude and their microphysical properties, such as particle size distribution and particle shape which in turn depend on the temperature, pressure, super-saturation conditions and existence or absence of nucleating particles. Indeed, the Ci cloud radiative effect (CCRE) at TOA have been widely studied using satellite data (e.g., Futyán et al., 2005; Harries et al., 2005; Choi et al., 2006), showing that the shortwave (SW) CCRE produces a cooling effect depending on cloud cover, COD and solar zenith angle (SZA) (i.e., Chen et al., 2000; Futyán et al., 2005). However, their net effect (i.e., SW CCRE + longwave (LW) CCRE) at TOA is potentially to get a positive sign. In particular, Chen et al. (2000) reported a net CCRE value of around +5.4 W m⁻², which is slightly higher than that obtained by Campbell et al (2016) (+0.67 W m⁻²), and additionally, a SW CCRE at surface of -22 W m⁻². In the works of Shupe and Intrieri (2004) and Dong et al. (2006) it was shown that the SW CCRE decreased about -1 Wm⁻² as the cloud cover increased (per percent of cloud fraction); in
115 addition, they indicated the SW CCRE on surface was mainly affected by both the SZA and surface

albedo, varying between -3 and -37 Wm⁻². Dupont and Haeffelin (2008) established that the SW CCRE on surface also depended on the AOD and humidity levels observed between the Ci altitude and the surface. Also, in that work, averaged SW CCRE values on surface were estimated for subvisual, semitransparent and opaque Ci clouds, obtaining, respectively, from -6 to -18 Wm⁻², -40 Wm⁻² and <-100Wm⁻². This can reflect the potentially relevant contribution of the SW CCRE to the net (SW+LW CCRE) radiative balance. Regarding the Ci cloud altitudes reported in those studies, it can be expected that the examined Ci clouds are composed by a mixture of water droplets and ice crystals. In the present work, Ci clouds composed mostly of ice particles are analysed, hence discriminating their effect from that of lower 'warmer' Ci clouds.

Additionally, desert dust storms and perhaps minor Aeolian emissions could play an important role on the formation of Ci clouds by acting dust as ice-nucleating particles (INPs) (e.g., Mamouri and Ansmann, 2016), which could be formed at higher than those expected temperatures by heterogeneous ice formation processes (deMott et al., 2015; Ullrich et al., 2017). Hence, Ci clouds can also indirectly modulate the radiative balance of the Earth, being especially relevant for those observed at mid-latitudes. For instance, recent analyses suggest that mineral dust particles transported from Saharan and Asian deserts are also effective INPs for initiating the formation of mid-latitude Ci clouds, as recently monitored with ground-based LIDAR techniques above Sofia, Bulgaria (Deleva et al., 2019). Other recent LIDAR studies of Ci clouds at mid-latitudes have focused mostly on investigating the transport of the air mass that gives rise to Ci clouds (Keckhut et al., 2005). This campaign demonstrated that ice clouds could appear in the mid-latitude stratosphere when subtropical upper tropospheric moist air is transported quasi-isentropically into the mid-latitude lower stratosphere through thin filamentary structures.

One of the purposes of this study is to define a monitoring methodology that uses LIDAR observations at mid-latitudes devoted to continuous measurements of both Ci clouds and Saharan dust to evaluate their radiative impact, either direct, by separating both effects, or indirect, due to the dust-cloud interactions (i.e., INP studies). This methodology shall be first defined in this work for the first scenario, namely, focusing on the radiative properties of pure ice Ci clouds. Future work will be addressed to Ci clouds potentially formed during Saharan dust events.

Cirrus clouds are usually classified in three categories according to their Cloud Optical Depth (COD), τ_{CC} , as regarded in Córdoba-Jabonero et al. (2017) (adapted from Sassen et al., 1989; and Sassen and Cho, 1992): subvisual (svCi, τ_{CC} , < 0.03, as a conservative threshold for the visible Ci detection in the zenith); semitransparent (stCi, τ_{CC} : 0.03-0.30, also named optically-thin clouds), and opaque or optically-dense (opCi, τ_{CC} : 0.30-3.0) clouds. In order to analyse the particular radiative impact of each Ci COD-type group, three cases of Ci clouds observed at daytimes over ARN/Huelva between October 2016 and September 2017 were selected depending on their predominant COD observed along the day. In particular, a svCi episode occurred on 01 October 2016, stCi clouds observed on 08 May 2017, and opCi clouds detected on 28 October 2016 were examined.

The aim of this work is to evaluate the Cirrus Cloud Radiative Effects (CCRE) within the shortwave solar spectral band (SW: 300-4000 nm) at two climate-relevant height-levels: the top-of-atmosphere (TOA) and on surface (SRF). Moreover, the CCRE will be also examined in the SW spectral sub-intervals: ultraviolet (UV: 300-400 nm), visible (VIS: 400-700 nm) and near-infrared (NIR: 700-4000 nm) depending on the COD of the Ci clouds. In particular, this study will be focused on their dependence of the predominant COD-type Ci case. Therefore, the optical, macrophysical and bulk-related microphysical properties of three principal optical categories of Ci clouds (Sassen et al., 1989; Sassen and Cho, 1992) as observed over the mid-latitude El Arenosillo station at Huelva (ARN/Huelva, south-western Iberian Peninsula) are analysed. In addition, their relationship with their Ice Water Path (IWP) and the effective radius of the ice particles will be also addressed. Results can represent a good reference for on-going long-term Ci observations at

ARN/Huelva site, and thus contribute to validation purposes of the next ESA/EarthCARE mission (launching scheduled for 2021), whose scientific goals are especially related to the aerosol-cloud-radiation interactions.

170

2. SITE, INSTRUMENTATION AND DATA

2.1. Measurement station

The El Arenosillo station is located close to Huelva (ARN/Huelva) at the South-western Iberian Peninsula (SW IP, 37.1°N 6.7°W, 40 m a.s.l.), enclosed in a rural protected environment nearby the Doñana National Park, less than 1 km from the Atlantic coastline. **Figure 1** illustrates the map showing the relative geolocation of the observatory. ARN/Huelva is managed by the Atmospheric Research and Instrumentation Branch of the Spanish Institute for Aerospace Technology (INTA), devoted to the monitoring and research of aerosols/clouds and gases using both remote sensing and in-situ instrumentation, together with solar radiation observations.

175
180 The aerosol background at ARN/Huelva is mostly from marine and rural origin. Dust intrusions are also usually frequent due to its close proximity to the African continent and the Saharan desert sources, especially in summertime. Hence, dust particles represent a key type of aerosols widely investigated at ARN/Huelva (i.e., Toledano et al., 2007; Córdoba-Jabonero et al., 2011; Sorribas et al., 2017). In this context, ARN/Huelva is representative of rural/coastal background conditions usually affected by Saharan dust particles.

185



Figure 1. The environment of El Arenosillo station (ARN/Huelva), located at the Southwest Iberian Peninsula (37.1° N 6.7° W, 40 m a.s.l.). Both the radiation instrumentation and the lidar system are also marked in red, separated around 100 m distance.

190

One of the recently initiated research activities in ARN/Huelva is addressed to the study of the vertical radiative effects of aerosols and clouds. In this work, the aim is focused on Cirrus (Ci) clouds observed at mid-latitudes, using both measurements and simulations.

195 2.2 LIDAR observations

A polarized Micro-Pulse Lidar (P-MPL, Sigma Space Corp.) was deployed in October 2016 at ARN/Huelva for vertical monitoring of aerosols and clouds. ARN/Huelva is both a NASA/AERONET (Aerosol Robotic Network, <https://aeronet.gsfc.nasa.gov/>) and NASA/MPLNET (Micro-Pulse Lidar Network, <https://mplnet.gsfc.nasa.gov/>) site. P-MPL routine measurements follow the MPLNET

200 requirements of 1-min integrating time and 15-/75-m vertical resolution (Welton et al., 2001). The P-MPL system is an elastic lidar that obtains vertical aerosol profiles with highly-pulsed (2500 Hz) and low-energy (7 μ J) Nd:YLF laser at 532 nm, operating in a full-time continuous (24/7) mode. The telescope is 5° tilted off the zenith to avoid normal reflection from ice clouds. Depolarization measurements are acquired from both the co- and cross-channel signals, $P_{co}(z)$ and $P_{cross}(z)$, respectively (z denotes the range/height dependence); the parallel and perpendicular range-corrected signals, $P^{||}(z)$ and $P^{\perp}(z)$, respectively, are obtained by adapting the methodology described in Flynn et al. (2007), using the expressions (hereafter, the range/height dependence is omitted for simplicity):

$$P^{||} = P_{co} + P_{cross} \quad (1)$$

210 and

$$P^{\perp} = P_{cross}. \quad (2)$$

The total range-corrected signal (RCS), P , is expressed as

$$P = P^{||} + P^{\perp} = P_{co} + 2 P_{cross}. \quad (3)$$

215 Due to the variability of the Cirrus clouds, 1-min lidar P , $P^{||}$, and P^{\perp} profiles are 10-min averaged in order to obtain a relatively good signal-to-noise ratio without neglecting potential Cirrus variability. Thus, 144 P-MPL profiles can be potentially examined for a day. Nevertheless, for comparison with radiation issues, only profiles at daytimes are analysed.

220 P-MPL measurements are used to derive the optical properties (backscatter coefficients, extinction) and the macrophysical features (top and base height boundaries, geometrical thickness) of the Cirrus clouds by applying the procedure described in Córdoba-Jabonero et al. (2017). In particular, in this work, the lidar parameters examined for the Ci clouds are the backscattering ratio, R , and its normalized value, $R_{norm} = 1 - [1/R]$, which can be expressed as

$$R_{norm} = \frac{\beta_c}{\beta_m + \beta_c}, \quad (4)$$

225 where β_c and β_m are, respectively, the cloud and molecular backscatter coefficients; the volume linear depolarization ratio, δ^V , as described in Flynn et al. (2007), can be expressed as

$$\delta^V = \frac{P^{\perp}}{P^{||}}, \quad (5)$$

where the depolarization calibration constant is omitted, as it is equal to 1 for P-MPL systems (Córdoba-Jabonero et al., 2013); the Cirrus Cloud Optical Depth (COD), τ_{cc} , that is defined as

$$\tau_{cc} = \int_{z_{base}}^{z_{top}} \sigma_c dz, \quad (6)$$

230 where σ_c is the cloud extinction coefficient, and z_{top} and z_{base} are, respectively, the top and base height-boundaries of the Ci cloud; the vertical extent (i.e., the geometrical thickness: $\Delta z = z_{top} - z_{base}$); and the Lidar Ratio (LR), S_{cc} , defined as

$$S_{cc} = \frac{\sigma_c}{\beta_c}. \quad (7)$$

235 As result of the methodology used (Córdoba-Jabonero et al., 2017; and references therein), note that the derived COD (and σ_c) and LR are 'layer-effective' variables, i.e., they represent a rather good approximation of those actual values for the Ci cloud layers examined in this work. That retrieval procedure is based on the transmittance method (i.e., Young, 1995; Chen et al., 2002; Platt et al., 2002), which is used to derive, in particular, the effective extinction profiles (and the corresponding COD), and also the effective LR of Cirrus clouds. The applicability of this method is based on aerosol-free (clean) conditions below and above the surroundings of the cloud. This can
240 be stated by looking at the rather homogeneous δ^V values found, indicating a low variability

inside the Ci clouds, and no presence of aerosols (no aerosol signature in δ^V profiles) below and above the Ci clouds (for instance, see **Fig. 2**). In addition, regarding the errors as estimated for COD and LR, uncertainties of 15-20% and 25-50% are obtained, respectively, corresponding the largest of those values to svCi cloud retrievals. It must be taken into account that in the retrieval procedure used to obtain the COD of the Cirrus clouds (Córdoba-Jabonero et al., 2017), data were filtered regarding their uncertainties, i.e., COD values (and hence their corresponding profiles) with uncertainties $> 30\%$ (usually obtained for the lowest CODs) were removed from the analysis and calculations performed. Thus, this ‘filtering’ proxy mostly affected the svCi category; however, a COD value of 0.0027 ± 0.0006 was derived as the lowest value within the selected Ci cases examined in this study. That particular value can be considered as the minimal COD threshold of the retrieval method used in this work.

Moreover, the criterion applied to determine the Ci cloud boundaries, defining the vertical extension of the Ci layer, was slightly modified w.r.t the retrieval described in Córdoba-Jabonero et al. (2017), taking also into account depolarization measurements. Indeed, Ci clouds, as composed mainly of ice particles, are highly depolarizing, presenting large δ^V values in the range of 0.30-0.50; hence, δ^V , together with R_{norm} , is usually used for determining pure ice clouds. In particular, δ^V as obtained from P-MPL measurements was validated against space-borne CALIPSO (Cloud-Aerosol Lidar and Infrared Pathfinder Satellite Observation, www.calipso.larc.nasa.gov) observations (Winker et al., 2009) of polar stratospheric clouds, which were purely composed of ice particles (Córdoba-Jabonero et al., 2013), showing P-MPL-derived δ^V and R_{norm} values higher than 0.30 and 0.9, respectively.

In this work, the Ci signature was referred to lidar-derived backscatter signals in the altitude range from 7 km height up to the tropopause. The z_{base} was obtained from the δ^V profile to discard the detection of no-ice clouds (low depolarization: $\delta^V < 0.01$), which are usually located below the Ci clouds. It was determined as the maximal height below the cloud that fulfils δ^V is less than a given threshold value, δ_{th}^V . For each particular Ci case, δ_{th}^V was experimentally identified at day- (dt) and night-times (nt), hence obtaining the following δ_{th}^V values, respectively: 0.070 (dt) and 0.040 (nt) on 01 October 2016, and 0.040 (dt) and 0.025 (nt) on 28 October 2016 and 08 May 2017. The daytime δ_{th}^V are higher than those nighttime values due to the solar background, leading to the signal-to-noise ratio (SNR) reduction. In addition, as height increases as the SNR for δ^V also decreases, z_{top} is obtained from the P profile, and defined as the minimal height above the cloud where P is less than its corresponding value at z_{base} (i.e., $P < P(z_{base})$). Once identified z_{base} and z_{top} , both the COD and LR of the Ci clouds, τ_{cc} and S_{cc} , respectively, can be derived by applying the methodology as described in Córdoba-Jabonero et al. (2017). Moreover, multiple scattering (MS) effects depend on the lidar field-of-view (FOV), the distance between the lidar and the scattering target and the particle size and density (Bissonnette, 2005). Therefore, due to the narrow FOV of the P-MPL system (100 μ rad) these MS effects were neglected in τ_{cc} and S_{cc} retrievals (Lewis et al., 2016).

An additional criterion is also used to confirm the detection of Ci clouds. That is based on the temperature at the top boundary of the cloud, $T_{top} = T(z_{top})$, which must be lower than the threshold of -37°C given for ice cloud formation (Campbell et al., 2016). Unfortunately, local radiosoundings were unavailable for the selected Ci-detected days. Temperature profiles were obtained from GDAS (Global Data Assimilation System) meteorological profiles as provided from the NOAA/READY (Real-time Environmental Applications and Display sYstem, www.ready.noaa.gov/READYamet.php) site (Rolph et al., 2017; READY, 2020) for the same selected Ci-detected days over the ARN/Huelva station. **Table 1** shows both the height and temperature of the tropopause, z^{tropo} and T^{tropo} , respectively, and the altitude at which the temperature threshold of -37°C (z^{-37}) is reached, as obtained from GDAS temperature profiles.

290

Table 1. Both the height (z^{tropo} , km) and temperature (T^{tropo} , °C) of the tropopause and the altitude at which the temperature threshold of -37°C is reached (z^{-37} , in km), as obtained from GDAS temperature profiles.

Ci case	z^{-37}	z^{tropo}	T^{tropo}
svCi 01 October 2016	9.4	14.0	-65.1
stCi 08 May 2017	9.2	13.9	-67.2
opCi 28 October 2016	9.3	14.9	-67.7

295

2.3 Solar radiation measurements

Long-term ozone and solar radiation measurements are carried out at ARN/Huelva. The longest observational series for total ozone content are being recorded since 1980 with the Dobson#120 instrument and since 1997 using a double Brewer system, establishing the ARN/Huelva as the station #213 of the Global Ozone Observing System of the World Meteorological Organization (WMO). ARN/Huelva is also equipped with instrumentation measuring the solar radiation, either detached into the global, direct and diffuse components or registered within specific spectral bands. Moreover, the ARN/Huelva calibration radiation laboratory has become an international reference for radiometric measurements, sharing protocols with the World Radiation Center (WRC, Davos, Switzerland). Performing an adequate calibration of the solar instruments and following quality assurance and quality control (QA/QC) procedures is crucial in order to obtain high-quality data (i.e., Vilaplana et al., 2009; Egli et al., 2016). Indeed, the ARN/Huelva solar instrumentation has been supported by using those calibration and QA/QC protocols. In this sense, the ARN/Huelva station is worldwide acknowledged for having the best reference solar instrumentation, being regularly used as an international intercomparison centre for instruments measuring total ozone column and solar radiation, including also sky cameras for the determination of cloudiness.

The solar radiation data used in this work were obtained by a set of radiometers installed on a Kipp&Zonen 2AP solar tracker in the rooftop of the main building in the ARN/Huelva observatory (see Fig. 1), about 100 m distance from the lidar observations. The Global (G) and Diffuse (D) radiations were measured by using two Kipp&Zonen CMP11 pyranometer (spectral range: 285 - 2800 nm), shadowing the one measuring the diffuse component. A Kipp&Zonen SHP1 pyrhelimeter (200 - 4000 nm) was used to measure the Direct (I) component of the solar radiation. Data were also 10-min averaged, as for the lidar profiles. That instrumentation is regularly calibrated with traceability to the World Radiation Reference (Hülßen et al., 2008; Vilaplana et al., 2009).

The whole sky dome images are obtained from an All-Sky Imager located at approximately 100 m distance to the north from the lidar system. The All-Sky Imager is an adaptation of a scientific CCD camera together with a digital colour video camera with a fish-eye lens (180° FOV) pointing to the zenith. In addition, the camera is protected from the direct solar radiation by a solar-shadow system with the purpose of avoiding the direct Sun incidence on the lens. These images are used to corroborate the presence of Ci clouds on those selected days.

3. METHODOLOGY

3.1 Cirrus Cloud Radiative Effect (CCRE)

In order to determine the influence of the Cirrus clouds to the radiative balance of the atmosphere, simulations of the solar radiation levels were performed using a radiative transfer (RT) model, the pseudo-spherical SDISORT code (Dahlback and Stammes, 1991), included in the LibRadtran software package (Mayer and Kylling, 2005). The radiative impact of the Cirrus clouds is determined in terms of the so-called Cirrus Cloud Radiative Effect (*CCRE*) at two climate-relevant altitudes: TOP-of-Atmosphere (TOA) and on the surface (SRF); the atmospheric *CCRE* ($CCRE^{atm}$), which is defined as the radiative impact of the Ci clouds in the overall atmosphere, was also estimated. The Ci-related input data to the model are both the lidar-derived extinction coefficient profiles of the Ci clouds, σ_c (and also τ_{cc}), and their height boundaries, z_{top} and z_{base} , as retrieved using the methodology described in **Sect. 2**. In particular, in order to extent the COD-dependence results on *CCRE* estimation, opCi cases were detached into two sub-cases depending on their COD: opCi-1 (τ_{cc} : 0.30-0.75) and opCi-2 (τ_{cc} : 0.75-3.00).

Similarly to the so-called Aerosol Radiative Effect (ARE) (namely also instantaneous Aerosol Radiative Forcing), which is an useful parameter widely used to determine the radiative impact of aerosols (i.e., particles) in the atmosphere (Antón et al., 2011; Mateos et al., 2014a; Sicard et al., 2014; Valenzuela et al., 2017; and references herein), the *CCRE* can be also defined for the Ci clouds in particular (i.e., Dupont and Haeffelin, 2008; Barja and Antuña, 2011) as

$$CCRE_x^z = (F_{CC}^\downarrow - F_{CC}^\uparrow) - (F_0^\downarrow - F_0^\uparrow), \quad (8)$$

where F is the simulated radiation flux ($W m^{-2}$), being spectrally-integrated within several spectral intervals, as denoted by x : the overall shortwave (SW: 250-4000 nm) range and specific SW ranges: ultraviolet (UV: 280-400 nm), visible (VIS: 400-700 nm) and near-infrared (NIR: 700-4000 nm). z stands for the selected height-levels (i.e., TOA and SRF), where F is calculated. Symbols \downarrow and \uparrow represent the downward and upward directions, respectively; hence, the downward F^\downarrow and upward F^\uparrow can be defined by the following expressions in terms of the global, G , and diffuse, D , components of the solar radiation:

$$F^\downarrow = G^\downarrow \quad (9)$$

$$F^\uparrow = D^\uparrow \quad (10)$$

In particular, $G^\downarrow = I \cos(\vartheta) + D^\downarrow$, being I the solar direct component, and ϑ the Solar Zenith Angle (SZA). G , I and D (upward and downward directions) radiation fluxes were calculated at 10-min intervals for SZAs up to 90° for the selected days. Finally, CC and 0 indicate the atmospheric conditions reproduced in the RT simulations, corresponding, respectively, to those found under the only presence of the Ci clouds, i.e., the optical and macrophysical properties of the Ci clouds (τ_{cc} , z_{top} , z_{base}) are introduced in the model, and under Ci cloud-free ($\tau_{cc} = 0$) but no aerosol-free conditions (the AOD can be not negligible, as shown in **Table 2**). Note that by applying the sign criterion of **Eq. (8)**, negative/positive *CCRE* values represent Ci cloud cooling/warming effects. Other authors also used the *CCRE*, as defined in **Eq. (8)**, as a measure of the radiative effect of the clouds in overall (i.e., Wacker et al., 2011; Mateos et al., 2013; Mateos et al., 2014b; Salueiro et al., 2014). In addition, $CCRE^{atm}$ can be also determined, following the expression

$$CCRE_x^{atm} = CCRE_x^{TOA} - CCRE_x^{SRF}. \quad (11)$$

As before, x stands for a specific spectral range (SW, UV, VIS, NIR). Wavelength integration within those spectral bands was performed using the correlated-k method (Kato et al., 1999). In order to introduce the spectral dependence of the Ci extinction in RT simulations, the single lidar-derived τ_{cc} at 532 nm was used to obtain the corresponding τ_{cc} at representative wavelengths for the SW, UV, VIS and NIR bands using the procedure described in **Sect. 3.2** next. In particular, spectral

375 RT simulations were integrated from 250 to 10000 nm for evaluation against surface radiation measurements; the spectral range extension until 10000 nm was calculated using data provided by Kurucz (1992).

380 Simulations were performed using the US standard atmosphere (Anderson, 1986) for mid-latitudes. Aerosol inputs were introduced in the RT retrieval using available AERONET V3 Level 2.0 data (AERONET, 2019) as provided at the ARN/Huelva site on those Ci days. The Aerosol Optical Depth (AOD) was 10-min averaged and interpolated, if necessary, along the day. Unfortunately, only L2.0 data were available for the asymmetry parameter, g , but not for the single scattering albedo (SSA), ω_0 (only L1.5 data); hence, restricted L1.5 ω_0 values to those coincident in time with the L2.0 g ones were used. By restricting SSA values, negligible differences (< 1%) in the mean ω_0 were observed on 28 October 2016 and 08 May 2017, being the highest one (around 5%) found on 1 October 2016; however, even though, that SSA difference introduced negligible changes in the CCRE as high as $\pm 0.02 \text{ W m}^{-2}$, which are within the corresponding errors. The ω_0 and g parameters presented a small, both spectral and temporal, variability during each Ci day; hence, daily-averaged ω_0 and g values at all the wavelengths were used for the simulations.

390 **Table 2** shows the aerosol input values used in RT simulations. Since the ARN/Huelva station is surrounded by a sea of pines next to a principal road, a surface albedo of 0.07 was applied, corresponding to the mean value between that for pines at short wavelengths (0.086, Betts and Ball, 1997) and that for asphalt (0.059, Turner and Parisi, 2018).

395 **Table 2.** AERONET V3 L2.0 daily-averaged AOD at 500 nm together with the SSA (ω_0) and asymmetry parameter (g) values used in RT simulations for each day.

Ci case	AOD	ω_0 (*)	g
svCi			
01 October 2016	0.12 ± 0.01	0.92 ± 0.02	0.65 ± 0.03
stCi			
08 May 2017	0.04 ± 0.01	0.85 ± 0.07	0.68 ± 0.01
opCi			
28 October 2016	0.21 ± 0.04	0.96 ± 0.03	0.73 ± 0.02

(*) ω_0 values correspond to AERONET V3 L1.5 data, but restricted to those coincident in time with AERONET V3 L2.0 g values.

400

3.2 Radiative parameters of the Cirrus clouds associated to their bulk-like microphysical properties

Radiative effects of the Cirrus clouds also depend on their microphysical properties. Indeed, small/large ice particles together with their concentration could produce low/high light scattering processes, modulating thus the atmospheric radiative balance. The size of ice particles is defined in terms of their effective radius, R_{eff} , and their concentration is related to the Ice Water Content (IWC , g m^{-3}) of the Ci clouds. In turn, both these characteristics depend on the mechanism of Cirrus formation, on the life stage of clouds, and are associated to the thermodynamics of the atmosphere (Krämer et al., 2016).

410 In order to introduce in the RT simulations a plausible R_{eff} value of the Ci (ice) particles, the relationship between their effective size and the atmospheric temperature, as reported in the

review work of Garrett (2008) on Cirrus synoptic clouds, is used to estimate, R_{eff} , as a first approximation; that is,

$$R_{eff} = 6 \times \exp[(T_m + 75)/35], \quad (12)$$

415 where T_m is a representative value of the temperature for the Ci cloud (in °C, being R_{eff} expressed in μm). Indeed, once both the top and base cloud altitudes are derived from P-MPL measurements, T_m can be obtained as an averaged value between these Ci boundaries of the temperature profile available from GDAS meteorological profiles (see **Sect. 2.2**).

420 Furthermore, Fu-parameterizations (Fu, 1996) are used for determining the Ice Water Content, IWC (g m^{-3}). It is widely reported in many works the generalized effective size, D_{ge} (μm), representing a measure of the ice crystal size; hence, D_{ge} , is calculated by modifying the Eq. (3.12) as shown in Fu (1996), expressing D_{ge} as a function of R_{eff} (μm), that is,

$$D_{ge} = \frac{8}{3(3)^{1/2}} R_{eff}. \quad (13)$$

425 Therefore, the IWC (g m^{-3}) can be obtained by introducing those D_{ge} values and the so-called effective cloud extinction, τ_{cc}^{eff} , in the following expression (as adopted from Eq. (3.9a) in Fu, 1996):

$$IWC = \frac{\tau_{cc}^{eff}}{[a_0 + (a_1/D_{ge})]}, \quad (14)$$

where

$$\tau_{cc}^{eff} = \tau_{cc} / \Delta z, \quad (15)$$

430 representing a first approximation for τ_{cc} as biased by the cloud geometrical thickness, Δz (m); and the a_i parameters ($i = 0, 1$) are the coefficients defined in Fu (1996) for the specific spectral bands where τ_{cc} was estimated. In this work, as τ_{cc} is derived from P-MPL measurements at 532 nm, $a_0 = -3 \cdot 10^{-5}$ and $a_1 = 2.5181$ (Fu, 1996). Hence, IWC (g m^{-3}) can be easily estimated from **Eq. (14)**.

435 In addition, the Ci radiative effects are influenced by the shape of the vertical distribution of R_{eff} and IWC (Feofilov et al., 2015). As we are interested in the bulk-like microphysical properties of the Ci clouds, the IWC can be assumed to be constant within the Ci layer (Guignard et al., 2012). Therefore, the results will be focused on the Ice Water Path, IWP (g m^{-2}), defined as the measure of the height-integrated IWC between the Ci cloud boundaries, that is,

$$440 \quad IWP = \int_{z_{base}}^{z_{top}} IWC(z) dz = IWC \Delta z, \quad (16)$$

assuming IWC constant. Those statements are justified regarding the small generalized effective sizes, D_{ge} , and low IWP values found in this work (see later, **Sect. 4.2** and **Table 3**). As Feofilov et al. (2015) reported, D_{ge} is rather constant for IWP less than 2 g m^{-2} , and is moderately higher close to the base boundary of the Ci layer for IWP ranging from 2 to 10 g m^{-2} . This is based on the low density of the ice particles ($\rho_{ice} = 0.9167 \text{ g cm}^{-3}$, Fu and Liu, 1993), which avoids the aggregation and buoyancy stratification within the Ci layer. However, for IWP higher than 30 g m^{-2} , the shape of the D_{ge} profile should be taken into account (Feofilov et al., 2015).

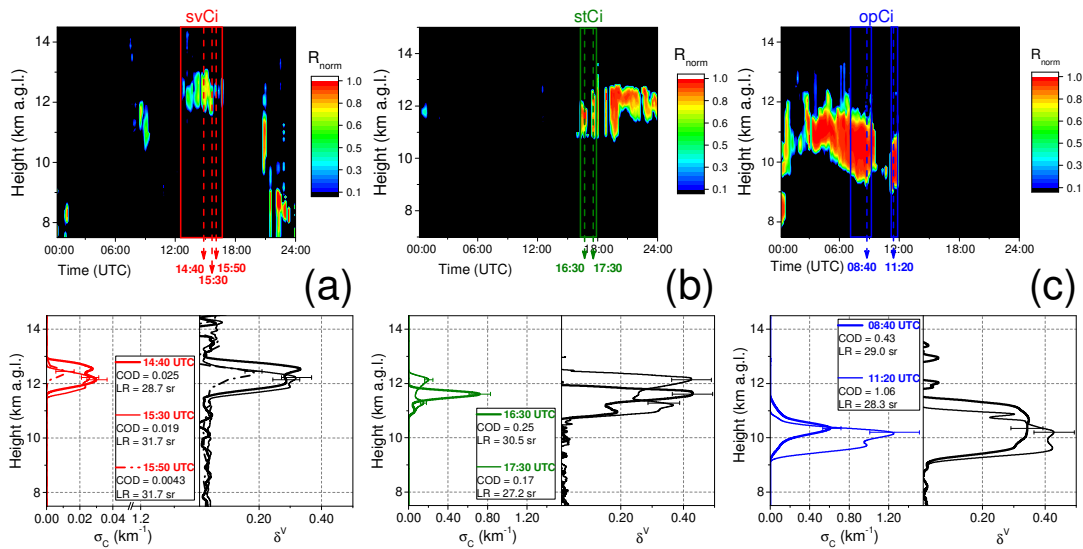
445 Once D_{ge} and IWP are known, τ_{cc} can be estimated at other wavelength ranges from **Eqs. (14-15)**, using the corresponding parameterized a_i coefficients as provided in Fu (1996) for each spectral range (as denoted by x in **Eqs. (8-11)**). Finally, those τ_{cc}^x are introduced in the RT model in order to obtain the simulated radiation fluxes (**Eqs. (8-10)**) for the overall SW interval, and the single UV, VIS and NIR bands, and also for the significant height-levels at TOA and SRF. Then, the diverse $CCRE$, as defined in **Sect. 3.1**, are calculated.

455 **4. RESULTS**

4.1. Optical properties and macrophysical features of Ci clouds

Ci clouds observed at ARN/Huelva have been examined for three days as representatives for each COD-type Ci cloud predominately detected. Regarding their occurrence, 26 Ci cases (1 case stands for a 10-min averaged profile) were observed on 01 October 2016 (early autumn), corresponding
 460 77% of them to subvisual Ci clouds (svCi) (20 cases); 31 out of 36 Ci cases (86%) detected on 08 May 2017 (spring) were identified as semitransparent Ci clouds (stCi); and a 67.3% of Ci cases (33 out of 49) observed on 28 October 2016 (autumn) were classified as opaque Ci clouds (opCi). As stated before, only Ci clouds detected at daytimes are examined for comparison with solar radiation issues; that is, 19 (95%), 7 (22.6%) and 17 (51.5%) cases of, respectively, SvCi, stCi and
 465 opCi clouds were analysed. For all those cases, their optical (COD, LR) and macrophysical (top and base height boundaries and vertical extent) properties were derived (see Sect. 2).

Figure 2 (top panels) shows the daily evolution of the Ci clouds observed over the ARN/Huelva station for each day in terms of the normalized backscattering ratio, R_{norm} (see Eq. (4)). Daytime svCi, stCi and opCi cases are marked between coloured (red, green and blue, respectively) solid lines.
 470 svCi are observed in two time ranges: 08:20-09:00 and 13:10-16:30 UTC (around 4.5 hours long, 19 profiles) (see Fig. 2a); on 08 May 2017, only seven stCi profiles could be derived at daytimes, mainly in the intervals 16:10-16:30 and 17:20-17:30 UTC (around for 50 minutes and for $SZA < 70^\circ$) (see Fig. 2b), and two later single cases observed at 18:40 and 19:10 UTC; and opCi were detected on 28 October 2016 from 07:00 to 09:00 UTC and from 11:10 to 11:40 UTC (17 profiles) (see Fig. 2c). **Table 3** summarizes the mean values and their standard deviations of: COD (τ_{CC}), LR (S_{CC} , sr), both the top and base height boundaries (z_{top} and z_{base} , km), and the vertical extent (geometrical thickness, Δz , km) for each COD-predominant Ci group. In addition, the mean temperatures ($^\circ\text{C}$) at z_{top} and z_{base} altitudes, T_{top} and T_{base} , respectively, of the Ci clouds is also included for the three case studies.
 475



480 **Figure 2.** Cirrus (Ci) clouds observed on: (a) 01 October 2016, (b) 08 May 2017, and (c) 28 October 2016 at the El Arenosillo station (ARN/Huelva). (Top panels) Contour plots of the vertical normalized backscattering ratio (R_{norm}) along the day; the predominant COD-type Ci clouds are also marked by coloured time intervals: svCi in red, stCi in green, and opCi in blue, and the particular profiles shown in the bottom panels are also indicated (by coloured dashed arrows).
 485 (Bottom panels) Those selected (in top panels) profiles of the extinction coefficient (σ_c , km^{-1}) and

the corresponding linear volume depolarization ratio (δ^V). Their lidar-derived COD (τ_{cc}) and LR (S_{cc}) values are also included in the legend.

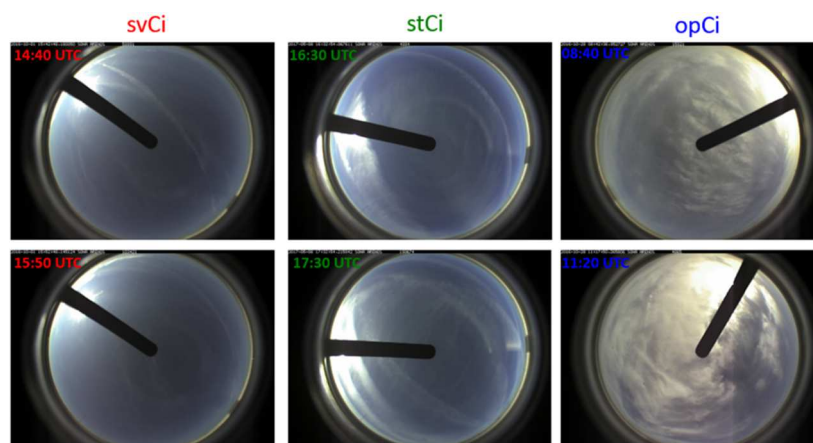
490 Mean S_{cc} values (25 - 35 sr) are within the typical LR range for Ci clouds, being the lowest values
 (~ 25 sr) for the svCi cases. Note that multiple scattering effects are neglected in this work
 (otherwise, τ_{cc} and S_{cc} would be lower than those derived). These values are similar to those
 reported in Europe (Kienast-Sjögren et al., 2016) and Mediterranean area (Giannakaki et al.,
 2007). Regarding the altitude, svCi are detected at higher altitudes (their z_{top} is found around 13
 495 km height, just below the tropopause level, see **Table 3**) than the other two cases with z_{top} at
 around 12 and 11 km height, respectively, for the stCi and opCi clouds. Nevertheless, the vertical
 extent is similar for all the Ci cases, ranging between 1.7 and 2.0 km thickness. These results are
 in agreement with those found in Córdoba-Jabonero et al. (2017) for a relatively close station to
 ARN/Huelva. Moreover, the temperatures at z_{top} for the three cases were found to be lower than
 500 the threshold value (-37°C) for homogeneous ice cloud formation (i.e., Campbell et al., 2016). This
 indicates a complete ice phase for the Ci cloud particles. Higher differences were found between
 the T_{top} and T_{base} for the opCi clouds than for the other cases, with the T_{base} close to -37°C/-
 38°C. This could lead to a potential mixing with no-ice (liquid) particles for the opCi clouds.

505 **Table 3.** Mean optical and geometrical properties for the COD-predominant Ci group (N denotes
 the number of profiles examined for each Ci type). τ_{cc} , S_{cc} , z_{top} , z_{base} , Δz , T_{top} and T_{base} stand
 for, respectively, the COD, the LR, both the cloud top and base height boundaries, the
 geometrical thickness, and both the temperatures at z_{top} and z_{base} . T_m is the representative
 temperature of the Ci clouds (see Eq. (12)). Their mean effective radius, R_{eff} (in μm , and also the
 510 generalised effective size, D_{ge}), and Ice Water Path, IWP (in g m^{-2}), are also included. Note that
 the opCi category is also detached into two sub-groups, opCi-1 and opCi-2.

Day	01/10/2016	08/05/2017	28/10/2016		
Ci group (N)	svCi (19)	stCi (7)	opCi (17)	opCi-1 (5)	opCi-2 (12)
	τ_{cc} : 0.01 - 0.03	τ_{cc} : 0.03 - 0.30	τ_{cc} : 0.3 - 3.0	τ_{cc} : 0.30 - 0.75	τ_{cc} : 0.75 - 3.00
τ_{cc}	0.015 ± 0.009	0.22 ± 0.08	0.93 ± 0.35	0.5 ± 0.1	1.1 ± 0.3
S_{cc} (sr)	25 ± 8	35 ± 11	34 ± 8	31 ± 10	35 ± 7
z_{top} (km)	13.1 ± 0.9	12.4 ± 0.3	11.2 ± 0.3	11.1 ± 0.3	11.2 ± 0.3
z_{base} (km)	11.2 ± 0.5	10.7 ± 0.1	9.2 ± 0.2	9.2 ± 0.2	9.2 ± 0.2
Δz (km)	1.9 ± 0.8	1.7 ± 0.3	2.0 ± 0.1	1.9 ± 0.1	2.0 ± 0.1
T_{top} (°C)	-62.0 ± 2.2	-61.4 ± 1.0	-54.2 ± 2.0	-53.5 ± 2.2	-54.5 ± 1.9
T_{base} (°C)	-52.2 ± 1.8	-50.9 ± 1.1	-38.2 ± 1.8	-37.7 ± 1.9	-38.4 ± 1.7
T_m (°C)	-57.1 ± 3.3	-56.1 ± 5.3	-46.2 ± 8.0	-45.6 ± 7.9	-46.4 ± 8.1
R_{eff} (μm)	10.0 ± 1.0	10.3 ± 0.2	13.7 ± 0.7	13.9 ± 0.8	13.6 ± 0.7
D_{ge} (μm)	15.5 ± 1.5	15.8 ± 0.4	21.1 ± 1.1	21.5 ± 1.2	20.9 ± 1.1
IWP (g m^{-2})	0.09 ± 0.05	1.4 ± 0.5	7.7 ± 2.8	4.4 ± 1.0	9.1 ± 2.1

515 Furthermore, among those Ci clouds observed, particular profiles were selected for each case in order to illustrate the vertical differences found between all those COD-type Ci categories. For instance, lidar-derived profiles of the extinction coefficient, σ_c (km^{-1}), and the linear volume depolarization ratio, δ^V , are shown in **Figure 2** (bottom panels, left and right, respectively) (times are also indicated for each profile together with their particular COD and LR values). It should be noted the breakdown of x-axis in **Figure 2a**, highlighting that τ_{cc} are about 1 order or less of magnitude lower for the svCi case than for the other two cases, meanwhile δ^V is similar for all the cases, mostly varying between 0.30 and 0.40 (**Fig. 2, bottom-right**). Regarding their heights, they are found just below the tropopause height-level (around 13.5 km height) for the three Ci categories. However, the mean heights of the svCi case corresponded to the highest altitudes ($z_{top} \sim 13$ km height) followed by the stCi ($z_{top} \sim 12$ km) and the opCi cases ($z_{top} \sim 11$ km) (see **Fig. 2, and Table 3**).

525 Images as collected by the all-sky camera sited on the terrace close to the radiation instrumentation at ARN/Huelva (see **Fig. 1**) represent a ‘visual’ illustration of the Ci clouds observed in the ARN/Huelva station during those days. Actually, they cannot directly be used to clearly distinguish a specific COD-type category. **Figure 3** shows a gradual occurrence (from left to right) of Ci clouds as detected at several times, coincident with those profiles shown in **Figure 2**, on 01 October 2016 (svCi), 08 May 2017 (stCi), and 28 October 2016 (opCi).



535 **Figure 3.** Images obtained with an all-sky camera at those times coincident with the detection of Ci clouds on: (Left) 01 October 2016 (svCi), (Centre) 08 May 2017 (stCi), and (Right) 28 October 2016 (opCi). For instance, times shown in each image correspond to the Ci profiles shown in **Fig. 2**.

4.2. Bulk-like microphysical properties of the Ci clouds

540 As mentioned above, Ci cloud-induced radiative effects are related to the effective size of the ice particles. Their size depends on several factors, but mainly on the atmospheric temperature (Feofilov et al., 2015; Krämer et al., 2016). The temperature threshold specified for ice cloud formation is $-37^\circ\text{C}/-38^\circ\text{C}$ at the top boundary of the Ci clouds (i.e., Campbell et al., 2016; Krämer et al., 2016).

545 Once the temperature fields were examined, the temperatures at the Ci top height-levels, T_{top} , for all Ci cases were found lower than the ice formation threshold of $-37^\circ\text{C}/-38^\circ\text{C}$ (see **Table 3**). Therefore, Ci clouds observed on the three cases are composed of ice particles (i.e., Campbell et al., 2016), which are assumed to be randomly oriented non-spherical hexagonal ice crystals. In these Ci scenarios, cloud radiative parameters, R_{eff} (and also D_{ge}) and IWP , were also estimated

550 (see **Sect. 3.2**). **Table 3** also shows the mean values obtained of those parameters for each predominant svCi, stCi and opCi (also, opCi-1 and opCi-2) groups.

For comparison with the values reported by other authors (i.e., Barja and Antuña, 2011), similar sizes are obtained for each Ci COD-type case; in average, R_{eff} ranged from $10.0 \pm 1.0 \mu\text{m}$ for svCi to $13.7 \pm 0.7 \mu\text{m}$ for opCi clouds, being $10.3 \pm 0.2 \mu\text{m}$ for stCi. These results just reflect the temperature dependence of R_{eff} (and D_{ge} , see **Eq. (13)**): slightly lower temperatures at Ci altitudes were detected on 01 October 2016 than those observed on the two other days, and accordingly showing smaller ice particles (Fu, 1996) for the stCi case, and then lower R_{eff} . Large differences between those values obtained for the three Ci cases were not found. For instance, a T_m of $-56 \pm 5^\circ\text{C}$ is reported for the stCi day, and -46 ± 8 and $-57 \pm 3^\circ\text{C}$ are found, respectively, for the opCi and svCi cases (see **Table 3**). On the other hand, *IWP* results reflect their clear direct dependence with the COD: as *IWP* enhances as R_{eff} increases, being similar their geometrical thicknesses (1.7 - 2.0 km). Indeed, *IWP* derived for the svCi, stCi and opCi clouds are, in average, 0.09 ± 0.05 , 1.4 ± 0.5 and $7.7 \pm 2.8 \text{ g m}^{-2}$ (4.4 ± 1.0 and $9.1 \pm 2.1 \text{ g m}^{-2}$ for opCi-1 and opCi-2 subgroups), respectively. Those *IWP* values are less than 2 g m^{-2} for svci and stCi clouds, and between 2 and 10 g m^{-2} for the opCi category; these results justify, as previously stated, the assumption of a homogeneously constant *IWC* along the Ci cloud layers observed in this work. However, the *IWP* (and also *IWC*) of the Cirrus clouds can be modulated under different Ci scenes: a different thermodynamic state of the atmosphere (temperature fields) together with a relative predominance of a given COD-type Ci cloud.

570

4.3. Cirrus cloud radiative effects

4.3.1 RT simulations against solar radiation measurements on surface under cloud-free conditions

In order to evaluate the radiative outputs of the RT model, simulations of the solar global radiation (SGR, W m^{-2}) of the totally-integrated SW solar spectrum reaching the ground were performed and compared to surface SGR measurements. The comparative analysis is based on the SGR differences, Δ (W m^{-2}), between the simulated (SGR_s) and measured (SGR_m) values in dependence of the solar zenith angle (SZA): $\Delta = SGR_s - SGR_m$. Two Ci cloud-free conditions were considered: clear and clean skies (clear mode) and no Ci presence (no-Ci mode). **Figure 4** shows the measured and simulated surface SGR levels for both Ci-free scenarios together with their differences, Δ . For the clear mode (see **Fig. 4a**), a day with predominately clear (mostly, no presence of low clouds) and clean (AOD < 0.01) conditions is selected: 15 October 2016. For the no-Ci mode, only aerosol features were introduced in RT simulations, and data corresponding to times with Ci cloud detection were disregarded. In this way, simulated radiation results obtained for each Ci day only reflect the effect of low clouds (no Cirrus) (see **Figs. 4b, 4c, and 4d**).

585

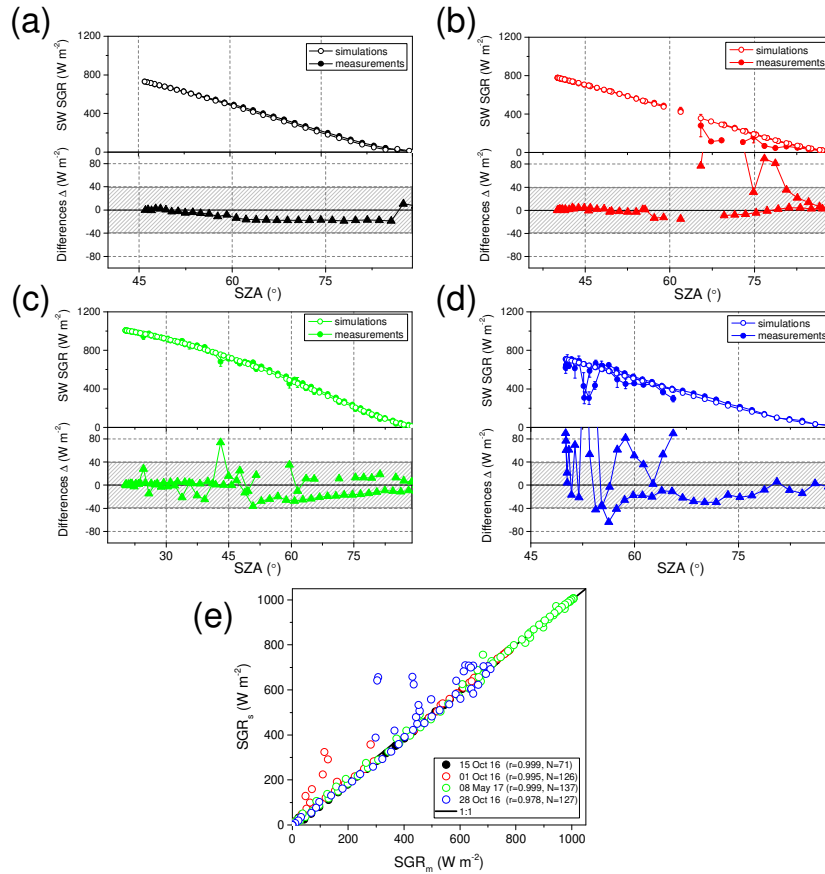


Figure 4. (Top panels, a-d) SW solar global radiation (SGR) levels measured on surface at El Arenosillo/Huelva station (full circles, and their error bars) and their corresponding RT simulations (no-Ci mode) (open circles) as a function of the Solar Zenith Angle (SZA): (a) during a mostly cloud-free and clean day on 15 October 2016 (black), and the three selected days with predominant COD-type Ci detection: (b) 01 October 2016 (svCi) (red), (c) 08 May 2017 (stCi) (green), and (d) 28 October 2016 (opCi) (blue), where the Ci features were removed; and (e) linear regression analysis of the SW SGR between simulations (SGR_s) and measurements (SGR_m), where the correlation coefficient, r , is shown within the legend for each day (N denotes the number of points used; coloured symbols correspond to those same as shown in the previous panels; and 1:1 line is also marked in black). (Bottom panels, a-d) SGR differences ($W m^{-2}$), $\Delta = SGR_s - SGR_m$ (full triangles) for those same days as shown in the top panels.

Ignoring a few cloud-screened features shortly observed on the SGR levels, differences in RT simulations under clear-mode conditions are within the $\pm 20 W m^{-2}$ interval (see **Fig. 4a**). Similar results are obtained for no-Ci-mode RT simulations: Δ are within $\pm 30 W m^{-2}$ for the svCi and stCi days and higher than that interval for the opCi day (see **Figs. 4b, 4c and 4d**). However, radiation levels are considerably reduced at SZAs higher than 75° ; discrepancies between simulations and measurements could be related to side effects due to instrumental geometrical reception. In addition, it is well known that the pseudo-spherical plane-parallel RT models, as the one used in this work, does not provide accurate results at high SZAs (Dahlback and Stammes, 1991). In overall, those differences could be based on the combination of both effects: the poorer resolution of the model for high SZAs and the cosine error of the broadband radiometers, which could be about 10% at SZAs $> 75^\circ$. Furthermore, the relevance of Ci clouds regarding their radiative effects for SZA $> 75^\circ$ is likely negligible (Shupe and Intrieri, 2004). In addition, linear regression analysis as performed between simulations and measurements provides correlation

coefficients, r , close to 1 for all the cases (see **Fig. 4e**, and the legend inside), even for the opCi case (**Fig. 4d**) where the presence of low clouds is clearly revealed. As a result, a rather good agreement of the RT simulations w.r.t. solar radiation measurements on surface for the two cloud-free modes is achieved, and hence the CCRE estimates (radiative effects under Ci occurrence: Ci mode) can be obtained using the RT model described in this work.

4.3.2 Ci-induced radiative effects at TOA and surface

The Cirrus cloud radiative effect, $CCRE$, has been obtained at two relevant height-levels: the top-of-atmosphere (TOA), $CCRE_x^{TOA}$, and on the surface (SRF), $CCRE_x^{SRF}$, where x indicates the spectral range within the RT simulations were performed (i.e., x : the overall SW range and their three UV, VIS and NIR bands, as described in **Sect. 3.1**, see **Eq. (8)**). The simulated radiation fluxes F_{CC}^{\downarrow} and F_0^{\downarrow} were retrieved, respectively, for the Ci- (Ci features introduced in the RT model) and no-Ci (no Ci signature considered) modes. **Figure 5** shows both the $CCRE_{SW}^{TOA}$ and $CCRE_{SW}^{SRF}$, and the atmospheric CCRE, $CCRE_{SW}^{atm}$, as a function of SZA ($< 80^\circ$) for each COD-type Ci case predominantly detected on those days (only the SW CCRE is shown for simplicity).

As expected, the CCRE at the TOA presents rather comparable negative values than those derived on the surface (SRF) for all the Ci categories at SW ranges (Chen et al., 2000). Those TOA/SRF CCRE values were ranging in the intervals ($[CCRE_{SW}^{TOA}]/[CCRE_{SW}^{SRF}]$): [-0.2, -3.5]/[-0.2, -3.6], [-10.8, -41.1]/[-10.8, -31.9] and [-35.8, -92.6]/[-26.1, -85.4] $W m^{-2}$, respectively, for the svCi, stCi and opCi categories; the atmospheric CCRE was within the ranges of [+0.3, -0.9], [+0.1, -9.1] and [-0.3, -28.7] $W m^{-2}$, respectively, for those same Ci groups. As the SW CCRE reveals, an enhanced cooling radiative effect is observed for the opCi clouds w.r.t. the other two Ci categories because of their higher COD. In addition, the $CCRE_{SW}^{atm}$ presents some positive, but low, values for svCi and stCi. In this sense, a more comprehensive analysis is performed on the COD-dependence of CCRE using the CCRE values for the overall SW interval and detached into their single UV, VIS and NIR bands (their corresponding mean CCRE values for each predominant Ci group are shown in **Table 4**).

The behaviour of the SW CCRE along with COD is shown in **Figure 6 (top panel)**; a similar variability is observed for the other spectral bands (UV, VIS and NIR; data are not shown for clarity). As exposed before, a similar pattern can be observed for both $CCRE^{TOA}$ and $CCRE^{SRF}$: as the COD increases as the cooling effect enhances, independently of the spectral range. However, the maximal Ci-induced cooling impact within the UV range is less than one order of magnitude w.r.t. to the total SW CCRE. Moreover, linear regression analysis for all the Ci cases detected at day-times (N=35) determined that higher negative increasing rates, as indicated by the slope of that linear fitting: ν ($W m^{-2} \tau^{-1}$), are found for the $CCRE$ at TOA than on the surface for all the SW spectral bands, showing also a high correlation coefficient, r . For instance, ν values for both $CCRE_{SW}^{TOA}$ and $CCRE_{SW}^{SRF}$ are -74 ± 4 $W m^{-2} \tau^{-1}$ ($r = 0.96$) and -55 ± 5 $W m^{-2} \tau^{-1}$ ($r = 0.90$), respectively; the $CCRE_{SW}^{atm}$ slightly decreased along with the COD increase, with a ν of -19 ± 2 $W m^{-2} \tau^{-1}$ and $r = 0.80$. Those corresponding ν and r values are also included in **Table 4**.

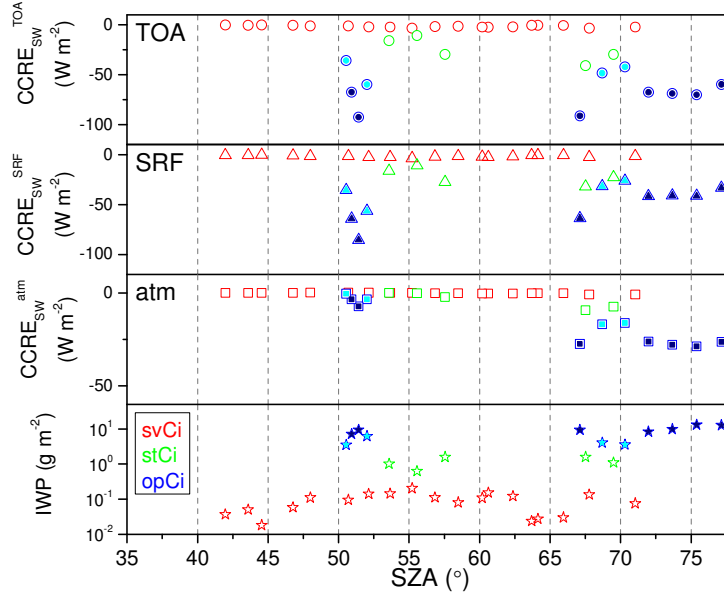


Figure 5. SW CCRE values ($W m^{-2}$) as estimated for the selected Ci cases as a function of the SZA at: (a) the top-of-atmosphere (TOA), $CCRE_{SW}^{TOA}$ (circles), and (b) on the surface (SRF), $CCRE_{SW}^{SRF}$ (triangles), together with (c) the atmospheric CCRE, $CCRE_{SW}^{atm}$ (squares), and (d) their corresponding IWP ($g m^{-2}$) (stars) for the three COD-type Ci clouds: svCi (red), stCi (green), and opCi (blue) cases. Note that the opCi category is also detached into two sub-groups, opCi-1 (cyan) and opCi-2 (dark blue), in dependence on their particular τ_{cc} range: 0.3-0.7 and 0.7-3.0, respectively.

655

660

By considering all the Ci clouds in overall, the mean SW CCRE values at TOA and SRF are, respectively, -30 ± 26 and $-24 \pm 19 W m^{-2}$, being the mean $CCRE^{atm} = -7 \pm 7 W m^{-2}$. These values are in good agreement with the global annual estimates found for Ci clouds, as defined with COD < 3.6 and their height base above 440 mb level in Chen et al. (2000): -25.3 , -22.2 , and $-3.1 W m^{-2}$ for the TOA, SRF and atmospheric CCRE, respectively. Campbell et al. (2016) showed similar $CCRE_{SW}^{TOA}$ negative values for each Ci-type category for clouds observed during one year at a mid-latitude site using the ice formation threshold of $-37^{\circ}C$ at the Ci top boundary as a proxy for Ci ice cloud discrimination. Our results are also in agreement with Dupont and Haeffelin (2008) that found a $CCRE_{SW}^{SRF}$ value of $-25 W m^{-2}$, considering only Ci clouds located above 11 km height. Dong et al. (2006) reported a higher value at surface ($-37.0 W m^{-2}$) for the mean annual average of high clouds; however, they defined high clouds as those with base height over 6 km, that is, including clouds rather composed by liquid water, whose cooling radiative effect is larger than that for ice clouds (Shupe and Intrieri, 2004).

665

670

The $CCRE_{SW}^{SRF}$ reported at the SIRTA observatory (25 km south from Paris) (Haeffelin et al., 2005) corresponded to Ci clouds observed for 23 days in the 2003-2006 period (Dupont and Haeffelin, 2008). They obtained a slope (ν value) of $-92 \pm 16 W m^{-2} \tau^{-1}$ using a linear fitting between $CCRE_{SW}^{SRF}$ and COD, with a correlation factor of $r = 0.79$. The $CCRE_{SW}^{SRF}$ values obtained in this work for svCi and stCi (-1.5 ± 0.9 and $-21.8 \pm 7.6 W m^{-2}$, respectively) are very close to those found when using the Dupont and Haeffelin's relationship (DHR). Regarding opCi-1 cases, the CCRE is also coincident with those values reported in Dupont and Haeffelin (2008), but only if errors are taken into account. However, the CCRE for the opCi-2 cases, corresponding to COD > 0.75, are notably lower (in absolute value, i.e., $-53 \pm 17 W m^{-2}$) than those provided by using DHR. This is due to the ν value found in this work ($-55 \pm 5 W m^{-2} \tau^{-1}$), which is lower (in absolute value) than that DHR-derived one. The main possible cause of these discrepancies can be associated to the

680

685 fact that Dupont and Haeffelin (2008) considered clouds with base heights from 7 km up, and a
potential presence of liquid water clouds could be introduced into the dataset. As mentioned
before, the radiative effect produced by those clouds is larger than that of ice clouds (Shupe and
Intrieri, 2004). In addition, by considering all types of clouds (water clouds included) as in the
690 study shown by Mateos et al. (2014b), a non-linear relationship was found between the cloud
radiative effect and the COD, where rather large COD values were examined. Regarding our
results, the obtained linear CCRE vs COD relationship can be accepted valid for ice Ci clouds,
which present rather low CODs in comparison with water clouds. In order to obtain reliable values
of the relationship between $CCRE_{SW}^{SRF}$ and COD, the study performed in this work should be
extended to a larger number of days with Ci detection, as planned in the future.

695

Table 4. Mean $CCRE$ values ($W m^{-2}$) at TOA and SRF, and the atmospheric CCRE, as obtained
within the overall SW interval and the single UV, VIS and NIR bands, for the COD-predominant Ci
group (their mean τ_{CC} is in parenthesis, see **Table 3**). Linear regression parameters for all the Ci
700 cases observed at day-times (N=35) describing the Ci cooling effect, i.e., both the negative
increasing rate (v , $W m^{-2} \tau^{-1}$) and the correlation coefficient (r), are also included.

Ci group	svCi (0.015 ± 0.009)	stCi (0.22 ± 0.08)	opCi (0.92 ± 0.35)	opCi-1 (0.50 ± 0.10)	opCi-2 (1.1 ± 0.3)	v	r
<i>CCRE</i> at the top-of-atmosphere (TOA): $CCRE_x^{TOA}$, where x :							
<i>SW</i>	-1.6 ± 1.0	-25.5 ± 10.8	-64 ± 17	-47 ± 9	-74 ± 12	-74 ± 4	0.96
<i>UV</i>	-0.07 ± 0.04	-0.9 ± 0.3	-2.3 ± 0.9	-1.8 ± 0.7	-2.6 ± 0.9	-2.9 ± 0.5	0.97
<i>VIS</i>	-0.6 ± 0.4	-9.4 ± 3.6	-23 ± 7	-17 ± 4	-26 ± 6	-27 ± 4	0.98
<i>NIR</i>	-0.9 ± 0.6	-15.2 ± 7.0	-38 ± 10	-27 ± 5	-45 ± 6	-43 ± 5	0.99
<i>CCRE</i> on surface (SRF): $CCRE_x^{SRF}$, where x :							
<i>SW</i>	-1.5 ± 0.9	-21.8 ± 7.6	-47 ± 17	-37 ± 12	-53 ± 17	-55 ± 5	0.90
<i>UV</i>	-0.06 ± 0.04	-0.8 ± 0.2	-2.0 ± 0.9	-1.6 ± 0.7	-2.2 ± 1.0	-2.5 ± 0.5	0.97
<i>VIS</i>	-0.6 ± 0.4	-9.0 ± 3.2	-20 ± 7	-16 ± 5	-23 ± 7	-24 ± 4	0.97
<i>NIR</i>	-0.9 ± 0.5	-12.0 ± 4.2	-25 ± 9	-20 ± 6	-28 ± 10	-30 ± 6	0.96
Atmospheric CCRE ($CCRE_x^{atm}$), where x :							
<i>SW</i>	0.07 ± 0.28	-3.7 ± 3.8	-17 ± 11	-9 ± 7	-21 ± 10	-19 ± 2	0.80
<i>UV</i>	-0.01 ± 0.01	-0.14 ± 0.10	-0.4 ± 0.2	-0.3 ± 0.1	-0.4 ± 0.1	-0.4 ± 0.1	0.99
<i>VIS</i>	0.00 ± 0.05	-0.4 ± 0.6	-2.9 ± 2.0	-1.6 ± 1.4	-3.7 ± 1.8	-3 ± 1	0.98
<i>NIR</i>	-0.07 ± 0.22	-3.2 ± 3.2	-13 ± 9	-7 ± 6	-17 ± 8	-15 ± 5	1.00

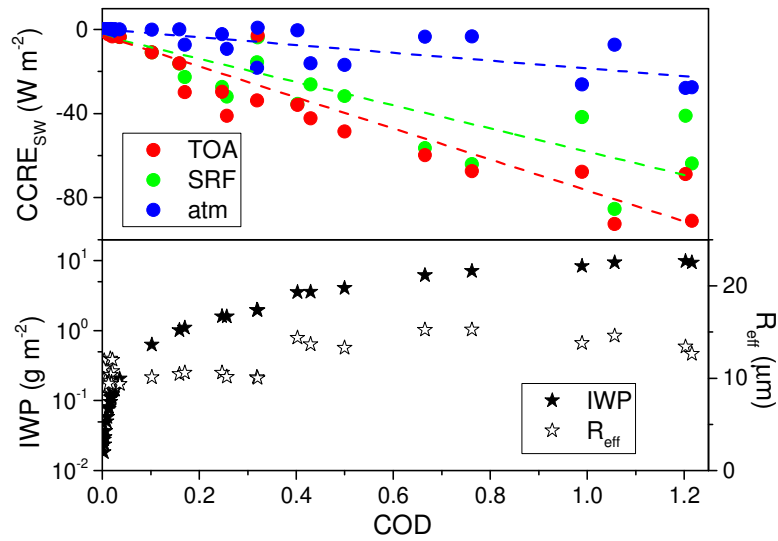


Figure 6. (Top) SW $CCRE$ values ($W m^{-2}$) as obtained at TOA (red) and SRF (green), and the atmospheric $CCRE$ (blue) for all the Ci cases in dependence with their particular COD (the corresponding values within the UV, VIS and NIR bands are shown in **Table 4**). Dashed lines represent the linear regression fitting performed for those three $CCRE$. (Bottom) the ice water path, IWP ($g m^{-2}$) (full stars), and the effective radius, R_{eff} (μm) (open stars), for all the same Ci cases within each Ci category: svCi, stCi, and opCi.

4.3.3 Ci-induced radiative effects related to the microphysical ice features of the Ci clouds

Cloud composition is an important factor for determining the radiative effect of clouds. Regarding their albedo at SW ranges, clouds containing liquid water strongly dominate w.r.t. ice clouds (Shupe and Intrieri, 2004). In that work, it is suggested that the cloud particle size is rather relevant on the albedo effect than the cloud phase one; water clouds are composed of small water droplets with a higher surface area per volume than that for large ice crystals. A comprehensive COD-dependence of the microphysical features of ice particles in Ci clouds in terms of their IWP and R_{eff} is illustrated in **Figure 6 (bottom panel)**. In particular, from svCi to opCi the IWP sharply increased almost 3 orders of magnitude, ranging from 0.02 (svCi) to 9.9 (opCi) $g m^{-2}$. In average for each predominant Ci group, IWP ranges from 0.09 ± 0.05 (svCi) to 9 ± 2 (opCi-2) $g m^{-2}$ (see **Table 3**). However, the effective radius R_{eff} slightly differed for all the Ci categories, i.e., in average, a R_{eff} of $12.0 \pm 1.8 \mu m$ is obtained (relative error: 15.1%) (see **Fig. 6, bottom panel**), as a result from the similar temperatures observed at those altitudes where Ci clouds were detected (see **Table 3**). Results as obtained for the IWP and R_{eff} values derived in this work are in good agreement with the ones reported by other authors. For instance, Barja and Antuña (2011) derived IWP values of 0.025, 1.2 and 18.4 $g m^{-2}$, respectively, for svCi, stCi and opCi clouds: our results are ranging in this same interval (see **Table 3**); meanwhile their R_{eff} values were found to be similar to those relatively large sizes for ice particles composing the Ci clouds observed in this work.

As expected, the behaviour of $CCRE$ is strongly dependent on the COD, and hence on IWP estimates, but it seems to be unrelated to the R_{eff} of ice particles of the Ci clouds examined in this work, where values are rather constant. Results reflect the fact that the IWP , and hence the ice water content, of the Ci clouds can be modulated depending on their COD and the temperature field of the atmosphere. In particular in this work, the COD is found to be the most

relevant Ci-induced parameter acting as a modulator proxy of the IWP, and hence the CCRE. However, this can change in different Ci cloud scenarios.

5. CONCLUSIONS

740 Cirrus (Ci) clouds were detected and characterized at the MPLNET El Arenosillo site in Huelva
(ARN/Huelva, SW Iberian Peninsula, 37.1°N 6.7°W) using the standard polarized Micro-Pulse Lidar
(P-MPL) system for the first time at this site. Lidar-derived optical (COD, LR) and microphysical
(top and base height-boundaries, geometrical thickness) properties of the Ci clouds were
745 retrieved for three COD-type Ci categories predominately detected during different days. A 77%
of the Ci cases observed on 01 October 2016 corresponded to subvisual Ci clouds (svCi);
semitransparent Ci clouds (stCi) were identified on 08 May 2017 (86% w.r.t. Ci cases detected);
and a 67% of Ci cases observed on 28 October 2016 were classified as opaque Ci clouds (opCi).
For comparison with solar radiation issues, only Ci clouds detected at daytimes were examined;
hence, 19, 7 and 17 cases were analysed, corresponding, respectively to svCi, stCi and opCi
750 clouds. The mean COD for each Ci category was, respectively, 0.02 ± 0.01 , 0.22 ± 0.08 and
 0.93 ± 0.40 ; in overall, their LR ranged between 25 and 35 sr. All-sky images collected for those
days showed a good coincidence with lidar observations of Ci clouds. They were detected
between 11 and 13 km height (top boundaries) with geometrical thicknesses of 1.7-2.0 km.
Temperatures at those altitudes corresponded to lower values than the thermal threshold for
755 homogenous ice formation ($-37^{\circ}\text{C}/-38^{\circ}\text{C}$), confirming a complete ice phase of the Ci clouds.
Additionally, lidar-derived values of R_{norm} higher than 0.9 and δ^V ranging between 0.3 and 0.4
also revealed Ci clouds mostly composed of ice particles. Moreover, the temperature fields were
also used together with Fu-parametrizations (Fu, 1996) to obtain the radiative-relevant
microphysical properties of the Ci clouds examined in this work, that is, the ice water path (IWP)
760 and the effective radius (R_{eff}) of the Ci ice particles. Results showed IWP values ranged from
0.02 to 9.9 g m^{-2} , from svCi to opCi clouds, with ice particles within the interval of 9-15 μm size.
These values are similar to those found in other Ci studies (i.e., Barja and Antuña, 2011).

The Ci cloud radiative effect (CCRE) was obtained by using a RT model to simulate the solar global
(direct + diffuse) radiation in two scenarios: under Ci-free conditions (no presence of Ci clouds)
765 and for the Ci-mode scene when the optical and microphysical properties of Ci clouds are
introduced into the model. As a first step, RT simulated outputs were evaluated against surface
solar radiation measurements carried out under relatively clean and cloud-free conditions.
Results revealed a good agreement between RT simulations and measurements, with correlation
coefficients close to 1, despite the presence of atmospheric screenings of low, potentially liquid,
770 clouds were not introduced in the simulations, and the different sky viewing between the solar
instrumentation (looking at a wider-averaged sky) and the lidar system (with a narrower field-of-
view). The CCRE was retrieved at the top-of-atmosphere (TOA) and on surface (SRF) for the overall
SW range and their single spectral UV, VIS and NIR bands. By considering all the Ci clouds,
independently on their COD, the mean SW CCRE values at TOA and SRF were, respectively, -
775 30 ± 26 and $-24 \pm 19 \text{ W m}^{-2}$, being the mean atmospheric CCRE of $-7 \pm 7 \text{ W m}^{-2}$. These values are in
good agreement with global annual mean estimates found for Ci clouds; however, if discrepancies
found, they can be associated to a probable presence of low liquid (small droplets) clouds in the
Ci dataset, likely producing a higher cooling effect than that associated to large ice crystal
particles of the Ci clouds.

780 By using linear regression analysis, a Ci-induced enhancing cooling radiative effect was observed
as COD increased for all the spectral ranges, with high correlation coefficients. In particular, the
SW CCRE at TOA and SRF, and the atmospheric CCRE, presented COD-dependent rates of -74 ± 4 ,
 -55 ± 5 , $-19 \pm 2 \text{ W m}^{-2} \tau^{-1}$, respectively. Additionally, increasing negative rates are found from UV to
NIR for each Ci category, reflecting a higher cooling NIR contribution w.r.t. UV and VIS ranges to

785 the SW CCRE, and being also more pronounced at the TOA w.r.t. on SRF, as expected. This is especially significant for space-borne photometric/radiometric instrumentation. Moreover, results reflect that the contribution of the SW CCRE to the net (SW+LW) radiative balance can be also potentially relevant.

790 In order to obtain more representative values of the quantities examined in this work, an extended dataset of Ci clouds must be used. However, the present study is indeed suitable to validate the method used for characterising the Ci clouds and their radiative effects. In this sense, results can contribute to validation purposes of the next ESA's EarthCARE mission, whose scientific goal is related to the radiation-aerosol-cloud interactions.

795 **Acknowledgements**

This work was supported by the Spanish Ministerio de Economía y Competitividad (MINECO) under grants CGL2014-55230-R (AVATAR), CGL2014-56255-C2-2-R (ICARO) and RTI2018-097332-B-C21 (NEFELE), in addition to the INTA13-1E-2696 (AERGAS) grant (Infraestructura cofinanciada con el Fondo Europeo de Desarrollo Regional (FEDER) "Una manera de hacer Europa"). Authors
800 acknowledge the support by the European Union's H2020 research and innovation programme through ACTRIS-2 project (GA 654109). Authors also thank the PIs of the AERONET El Arenosillo site and its personal staff for maintenance and operation support. The MPLNET project is funded by the NASA Radiation Sciences Program and Earth Observing System. Authors gratefully
805 acknowledge the NOAA Air Resources Laboratory (ARL) for the provision of the meteorological profiles from the READY website (<https://www.ready.noaa.gov>) used in this publication. L. Gómez-Martín thanks the MINECO support under grant CTM2013-41311-P and MCIU support under grant CTM2017-83199-P. A. del Águila thanks the MINECO support (Programa de Ayudas a la Promoción del Empleo Joven e Implantación de la Garantía Juvenil en i+D+i) under grant PEJ-2014-A-52129. M.-A. López-Cayuela is supported by the INTA training fellowship programme. M.-
810 P. Zorzano acknowledges the partial support of the Spanish State Research Agency (AEI) Project No. MDM-2017-0737 Unidad de Excelencia "María de Maeztu" - Centro de Astrobiología (INTA-CSIC).

Data availability

815 All data generated and analysed during this study are available from the corresponding author upon reasonable request.

References

820 AERONET: AERONET aerosol data base, available at <http://aeronet.gsfc.nasa.gov/>, last access: 21 May 2019.

Anderson, G.P., Clough, S.A., Kneizys, F.X., Chetwynd, J.H., and Shettle, E.P., 1986. AFGL atmospheric constituent profiles (0–120 km). Tech. rep. AFGL-TR-86-0110, Environ. Research papers No. 954.

825 Antón, M., Gil J.E., Fernández-Gálvez, J., Lyamani, H., Valenzuela, A., Foyo-Moreno, I., Olmo, F.J., Alados-Arboledas, L., 2011. Evaluation of the aerosol forcing efficiency in the UV erythemal range at Granada, Spain. *J. Geophys. Res.* 116, D20214. <https://dx.doi.org/10.1029/2011JD016112>.

Barja, B., Antuña, J.C., 2011. The effect of optically thin cirrus clouds on solar radiation in Camagüey, Cuba. *Atmos. Chem. Phys.* 11, 8625–8634. <https://doi.org/10.5194/acp-11-8625-2011>.

- 830 Betts, A.K., Ball, J.H., 1997. Albedo over the boreal forest. *J. Geophys. Res.* 102, D24, 28901-28909. <https://doi.org/10.1029/96JD03876>.
- Bissonnette, L.R., 2005. Lidar and multiple scattering. In Weitkamp, C. (Ed), *Lidar: Range-Resolved Optical Remote Sensing of the Atmosphere*. Springer, pp. 43–103.
- 835 Boucher, O., Randall, D., Artaxo, P., Bretherton, C., Feingold, G., Forster, P., Kerminen, V.M., Kondo, Y., Liao, H., Lohmann, U., Rasch, P., Satheesh, S.K., Sherwood, S., Stevens, B., Zhang, X.Y., 2013: Clouds and Aerosols, in: Stocker, T.F., Qin, D., Plattner, G.K., Tignor, M., Allen, S.K., Boschung, J., Nauels, A., Xia, Y., Bex, V., Midgley, P.M. (Eds.), *Climate Change 2013: The Physical Science Basis. Contribution of Working Group I to the Fifth Assessment Report of the Intergovernmental Panel on Climate Change*. Cambridge University Press, Cambridge, United Kingdom and New York, NY, USA.
- 840 Campbell, J.R., Vaughan, M.A., Oo, M., Holz, R.E., Lewis, J.R., Welton, E.J., 2015. Distinguishing cirrus cloud presence in autonomous lidar measurements. *Atmos. Meas. Tech.* 8, 435-449. <https://doi.org/10.5194/amt-8-435-2015>.
- 845 Campbell, J. R., Lolli, S., Lewis, J. R., Gu, Y., Welton, E. J., 2016. Daytime Cirrus Cloud Top-of-the-Atmosphere Radiative Forcing Properties at a Midlatitude Site and Their Global Consequences. *J. of App. Meteorol. Clim.* 55, 1667-1679. <https://doi.org/10.1175/JAMC-D-15-0217.1>
- Chen, T., W. B. Rossow, and Y. Zhang, 2000. Radiative effects of cloud-type variations. *J. Clim.*, 13, 264-286. [https://dx.doi.org/10.1175/1520-0442\(2000\)013<0264:REOCTV>2.0.CO;2](https://dx.doi.org/10.1175/1520-0442(2000)013<0264:REOCTV>2.0.CO;2).
- 850 Chen, W.N., Chiang, C.W., Nee, J.B., 2002. Lidar ratio and depolarization ratio for cirrus clouds. *Appl. Optics* 41, 6470–6476. <http://dx.doi.org/10.1364/AO.41.006470>.
- Choi, Y.S., Ho, C.H., 2006. Radiative effect of cirrus with different optical properties over the tropics in MODIS and CERES observations. *Geophys. Res. Lett.* 33, L21811. <https://doi.org/10.1029/2006GL027403>.
- 855 Córdoba-Jabonero, C., Sorribas, M., Guerrero-Rascado, J. L., Adame, J. A., Hernández, Y., Lyamani, H., Cachorro, V., Alados-Arboledas, L., Cuevas, E., and Morena, B., 2011. Synergetic monitoring of Saharan dust plumes and potential impact on surface: a case study of dust transport from Canary Islands to Iberian Peninsula. *Atmos. Chem. Phys.* 11 (7). <https://doi.org/3067-3091>. 10.5194/acp-11-3067-2011.
- 860 Córdoba-Jabonero, C., Guerrero-Rascado, J. L., Toledo, D., Parrondo, M., Yela, M., Gil, M., and Ochoa, H. A., 2013. Depolarization ratio of polar stratospheric clouds in coastal Antarctica: comparison analysis between ground-based Micro Pulse Lidar and space-borne CALIOP observations. *Atmos. Meas. Tech.* 6, 703-717. <https://doi.org/10.5194/amt-6-703-2013>.
- 865 Córdoba-Jabonero, C., Lopes, F.J.S., Landulfo, E., Cuevas, E., Ochoa, H., Gil-Ojeda, M., 2017. Diversity on subtropical and polar cirrus clouds properties as derived from both ground-based lidars and CALIPSO/CALIOP measurements. *Atmos. Res.* 183, 151-165. <https://doi.org/10.1016/j.atmosres.2016.08.015>.
- Dahlback, A., Stammes, K., 1991. A new spherical model for computing the radiation field available for photolysis and heating at twilight. *Planet. Space Sci.* 39, 671-683. [https://doi.org/10.1016/0032-0633\(91\)90061-E](https://doi.org/10.1016/0032-0633(91)90061-E).
- 870 Deleva, A.D., Peshev, Z.Y., Krasteva, E.N., Dreischuh, T.N., 2019. Simultaneous vertical LIDAR profiling of Saharan dust layers and high-altitude cirrus clouds in the troposphere. *Proc. SPIE* 11047, 20th International Conference and School on Quantum Electronics: Laser Physics and Applications, 1104712. <https://doi.org/10.1117/12.2516358>.
- 875 deMott, P.J., et al. 2015. Integrating laboratory and field data to quantify the immersion freezing ice nucleation activity of mineral dust particles. *Atmos. Chem. Phys.* 15, 393-409.

- Dong, X., Xi, B., Minnis, P., 2006. A climatology of midlatitude clouds from the ARM SGP Central Facility. Part II: Cloud fraction and surface radiative forcing. *J. Clim.* 19, 1765-1783. <https://doi.org/10.1175/JCLI3710.1>.
- 880 Dupont, J.C., Haeffelin, M., 2008: Observed instantaneous cirrus radiative effect on surface-level shortwave and longwave irradiances. *J. Geophys. Res.* 113, D21202. <http://doi.org/10.1029/2008JD009838>.
- Dupont, J.C., Haeffelin, M., Morille, Y., Noël, V., Keckhut, P., Winker, D., Comstock, J., Chervet, P., Roblin, A., 2010. Macrophysical and optical properties of midlatitude cirrus clouds from four ground-based lidars and collocated CALIOP observations. *J. Geophys. Res.* 115, D00H24. <http://doi.org/10.1029/2009JD011943>. 885
- Egli, L., Gröbner, J., Hülsen, G., Bachmann, L., Blumthaler, M., Dubard, J., Khazova, M., Kift, R., Hoogendijk, K., Serrano, A., Smedley, A., Vilaplana, J.M., 2016. Quality assessment of solar UV irradiance measured with array spectroradiometers. *Atmos. Meas. Tech.* 9, 1553-1567. <https://doi.org/10.5194/amt-9-1553-2016>.
- 890 Feofilov, A.G., Stubenrauch, C.J., Delanoë, J., 2015. Ice water content vertical profiles of high-level clouds: classification and impact on radiative fluxes. *Atmos. Chem. Phys.* 15, 12327-12344. <https://doi.org/10.5194/acp-15-12327-2015>.
- Flynn, C. J., Mendoza, A., Zheng, Y., Mathur, S., 2007. Novel polarization-sensitive micropulse lidar measurement technique. *Optics Express.* 15 (6), 2785-2790. <https://doi.org/10.1364/OE.15.002785>. 895
- Fu, Q., 1996. An accurate Parametrization of the Solar Radiative Properties of Cirrus Clouds for Climate Models. *J. Clim.* 9, 2058-2082. [https://doi.org/10.1175/1520-0442\(1996\)009<2058:AAPOTS>2.0.CO;2](https://doi.org/10.1175/1520-0442(1996)009<2058:AAPOTS>2.0.CO;2).
- 900 Fu, Q., and Liou, K. N., 1993. Parameterization of the Radiative Properties of Cirrus Clouds. *J. Atmos. Sci.* 50 (13), 2008-2025. [https://doi.org/10.1175/1520-0469\(1993\)050<2008:POTRPO>2.0.CO;2](https://doi.org/10.1175/1520-0469(1993)050<2008:POTRPO>2.0.CO;2).
- Futyan, J.M., Russell, J.E., Harries, J.E., 2005. Determining cloud forcing by cloud type from geostationary satellite data. *Geophys. Res. Lett.* 32, L08807. <https://doi.org/10.1029/2004GL022275>.
- 905 Garrett, T. J., 2008. Observational quantification of the optical properties of cirrus cloud, in: Kokhanovsky, A.A. (Ed), *Light Scattering Reviews 3*. Springer, Berlin, Heidelberg, pp. 3–26.
- Giannakaki, E., Balis, D.S., Amiridis, V., Kazadzis, S., 2007. Optical and geometrical characteristics of cirrus clouds over a Southern European lidar station. *Atmos. Chem. Phys.* 7 (21), 5519-5530. <https://doi.org/10.5194/acp-7-5519-2007>.
- 910 Guignard, A., Stubenrauch, C.J., Baran, A.J., Armante, R., 2012. Bulk microphysical properties of semi-transparent cirrus from AIRS: A six-year global climatology and statistical analysis in synergy with geometrical profiling data from CloudSat-CALIPSO. *Atmos. Chem. Phys.* 12, 503-525. <https://doi.org/10.5194/acp-12-503-2012>.
- 915 Haeffelin, M., L. Barthès, O. Bock, C. Boitel, S. Bony, D. Bouniol, H. Chepfer, M. Chiriaco, J. Cuesta, J. Delanoë, P. Drobinski, J.-L. Dufresne, C. Flamant, M. Grall, A. Hodzic, F. Hourdin, F. Lapouge, Y. Lemaître, A. Mathieu, Y. Morille, C. Naud, V. Noël, W. O'Hirok, J. Pelon, C. Pietras, A. Protat, B. Romand, G. Scialom, and R. Vautard, 2005. SIRTa, a ground-based atmospheric observatory for cloud and aerosol research. *Ann. Geophys.* 23, 2, 253-275. <https://doi.org/10.5194/angeo-23-253-2005>.
- 920 Harries, J.E., Russell, J.E., Hanafin, J.A., Brindley, H., Futyan, J., Rufus, J., Kellock, S., Matthews, G., Wrigley, R., Last, A., Mueller, J., Mossavati, R., Ashmall, J., Sawyer, E., Parker, D., Caldwell, M.,

- 925 Allan, P.M., Smith, A., Bates, M.J., Coan, B., Stewart, B.C., Lepine, D.R., Cornwall, L.A., Corney, D.R., Ricketts, M.J., Drummond, D., Smart, D., Cutler, R., Dewitte, S., Clerbaux, N., Gonzalez, L., Ipe, A., Bertrand, C., Joukoff, A., Crommelynck, D., Nelms, N., Llewellyn-Jones, D.T., Butcher, G., Smith, G.L., Szewczyk, Z.P., Mlynczak, P.E., Slingo, A., Allan, R.P., Ringer, M.A., 2005. The geostationary earth radiation budget project. *Bull. Am. Meteorol. Soc.* 86 (7), 945-960. <http://doi.org/10.1175/BAMS-86-7-945>.
- 930 Heymsfield, A., D. Winker, M. Avery, M. Vaughan, G. Diskin, M. Deng, V. Mitev, and R. Matthey, 2014. Relationships between ice water content and volume extinction coefficient from in situ observations for temperatures from 0 to -86°C: Implications for spaceborne lidar retrievals. *J. Appl. Meteorol. Clim.* 53, 479–505. <https://doi.org/10.1175/JAMC-D-13-087.1>.
- 935 Hülsen, G., Gröbner, J., Bais, A., Blumthaler, M., Disterhoft, P., Johnsen, B., Lantz, K.O., Meleti, C., Schreder, J., Vilaplana-Guerrero, J.M., Ylianttila, L., 2008. Intercomparison of erythemal broadband radiometers calibrated by seven UV calibration facilities in Europe and the USA. *Atmos. Chem. Phys.* 8, 4865-4875. <https://doi.org/10.5194/acp-8-4865-2008>.
- Kato, S., Ackerman, T.P., Mather, J.H., Clothiaux, E., 1999. The k-distribution method and correlated-k approximation for a shortwave radiative transfer model. *J. Quant. Spectrosc. Radiat. Transfer.* 62, 109–121. [https://doi.org/10.1016/S0022-4073\(98\)00075-2](https://doi.org/10.1016/S0022-4073(98)00075-2).
- 940 Keckhut, P., Hauchecorne, A., Bekki, S., Colette, A., David, C., Jumelet, J., 2005. Indications of thin cirrus clouds in the stratosphere at mid-latitudes. *Atmos. Chem. Phys.* 5, 3407-3414. <https://doi.org/10.5194/acp-5-3407-2005>.
- Kienast-Sjögren, E., Rolf, C., Seifert, P., Krieger, U.K., Luo, B.P., Krämer, M., Peter, T., 2016. Radiative properties of mid-latitude cirrus clouds derived by automatic evaluation of lidar measurements. *Atmos. Chem. Phys.* 16, 7605-7621. <https://doi.org/10.5194/acp-16-7605-2016>.
- 945 Krämer, M., Rolf, C., Luebke, A., Afchine, A., Spelten, N., Costa, A., Meyer, J., Zöger, M., Smith, J., Herman, R.L., Buchholz, B., Ebert, V., Baumgardner, D., Borrmann, S., Klingebiel, M., Avallone, L., 2016. A microphysics guide to cirrus clouds – part 1: cirrus types. *Atmos. Chem. Phys.* 16, 3463-3483. <https://doi.org/10.5194/acp-16-3463-2016>.
- 950 Kuhn, T., Heymsfield, A., 2016. In Situ Balloon-Borne Ice Particle Imaging in High-Latitude Cirrus. *Pure Appl. Geophys.* 173, 3065-3084. <https://doi.org/10.1007/s00024-016-1324-x>
- Kurucz, R.L., 1992. Synthetic infrared spectra, in: Rabin, D.M., Jefferies, J.T. (Eds), *Infrared Solar Physics*. Springer, Dordrecht, pp. 523-531.
- 955 Lewis, J.R., Campbell, J.R., Welton, E.J., Stewart, S.A., Haftings, P.C., 2016. Overview of MPLNET Version 3 Cloud Detection. *J. Atmos. Ocean. Techn.* 33, 2113-2134. <https://doi.org/10.1175/JTECH-D-15-0190.1>.
- Lolli, S., Campbell, J. R., Lewis, J. R., Gu, Y., and Welton, E. J., 2017a. Technical note: Fu–Liou–Gu and Corti–Peter model performance evaluation for radiative retrievals from cirrus clouds. *Atmos. Chem. Phys.* 17, 7025-7034. <https://doi.org/10.5194/acp-17-7025-2017>.
- 960 Lolli, S., Campbell, J.R., Lewis, J.R., Gu, Y., Marquis, J.W., Chew, B.N., Liew, S., Salinas, S.V., Welton, E.J., 2017b. Daytime Top-of-the-Atmosphere Cirrus Cloud Radiative Forcing Properties at Singapore. *J. Appl. Meteorol. Clim.* 56, 1249–1257. <https://doi.org/10.1175/JAMC-D-16-0262.1>.
- Mamouri, E., Ansmann, A., 2016. Potential of polarization lidar to provide profiles of CCN-and INP-relevant aerosol parameters. *Atmos. Chem. Phys.* 16, 5905–5931. <https://doi.org/10.5194/acp-16-5905-2016>.
- 965 Mateos, D., M. Anton, A. Valenzuela, A. Cazorla, F.J. Olmo and L. Alados-Arboledas, 2013. Short-wave radiative forcing at the surface for cloudy systems at a midlatitude site. *Tellus B*, 65, 21069, <https://doi.org/10.3402/tellusb.v65i0.21069>.

- 970 Mateos, D., Antón, M., Toledano, C., Cachorro, V.E., Alados-Arboledas, L., Sorribas, M., Costa, M.J., Baldasano, J.M., 2014a. Aerosol radiative effects in the ultraviolet, visible, and near-infrared spectral ranges using long-term aerosol data series over the Iberian Peninsula. *Atmos. Chem. Phys.* 14, 13497–13514. <https://doi.org/10.5194/acp-14-13497-2014>.
- Mateos, D., M. Anton, A. Valenzuela, A. Cazorla, F.J. Olmo and L. Alados-Arboledas, 2014b. Efficiency of clouds on shortwave radiation using experimental data. *App. Energy*, 113, 1216–1219, <http://doi.org/10.1016/j.apenergy.2013.08.060>.
- 975 Mayer, B. Kylling, A., 2005. Technical note: The libRadtran software package for radiative transfer calculations – description and examples of use. *Atmos. Chem. Phys.* 5, 1855–1877. <https://doi.org/10.5194/acp-5-1855-2005>.
- 980 Myhre, G., Shindell, D., Pongratz, J., 2013. Anthropogenic and natural radiative forcing. In: Stocker, T.F., Qin, D., Plattner, G.K., Tignor, M., Allen, S.K., Boschung, J., Nauels, A., Xia, Y., Bex, V., Midgley, P.M. (Eds.), *Climate Change 2013: The Physical Science Basis. Contribution of Working Group I to the Fifth Assessment Report of the Intergovernmental Panel on Climate Change*. Cambridge University Press, Cambridge, NY, USA.
- 985 Platt, C.M.R., Young, S.A., Austin, R.T., Patterson, G.R., Mitchell, D.L., Miller, S.D., 2002. LIDAR observations of tropical cirrus clouds in MCTEX. Part I: optical properties and detection of small particles in cold cirrus. *J. Atmos. Sci.* 59, 3145–3162. [http://dx.doi.org/10.1175/1520-0469\(2002\)059b3145:LOOTCCN2.0.CO;2](http://dx.doi.org/10.1175/1520-0469(2002)059b3145:LOOTCCN2.0.CO;2).
- READY (Real-time Environmental Applications and Display sYstem): READY data base, available at <https://www.ready.noaa.gov/READYamet.php>, last access: 03 February 2020.
- 990 Rolph, G., Stein, A., and Stunder, B., 2017. Real-time Environmental Applications and Display sYstem: READY. *Environmental Modelling and Software*, 95, 210–228. <http://dx.doi.org/10.1016/j.envsoft.2017.06.025>.
- Salgueiro, V., M. J. Costa, A. M. Silva and D. Bortoli, 2014. Variability of the daily-mean shortwave cloud radiative forcing at the surface at a midlatitude site in Southwestern Europe. *J. Clim.* 27, 7769–7780, <https://doi.org/10.1175/JCLI-D-13-00696.1>.
- 995 Sassen, K., Dodd, G.C., 1989. Haze particle nucleation simulations in cirrus clouds and applications for numerical and lidar studies. *J. Atmos. Sci.* 46(19), 3005–3014. [https://doi.org/10.1175/1520-0469\(1989\)046<3005:HPNSIC>2.0.CO;2](https://doi.org/10.1175/1520-0469(1989)046<3005:HPNSIC>2.0.CO;2)
- 1000 Sassen, K., Cho, B.S., 1992. Subvisual-thin cirrus lidar dataset for satellite verification and climatological research. *J. Ap. Meteorol.* 31 (11), 1275–1285. [https://doi.org/10.1175/1520-0450\(1992\)031<1275:STCLDF>2.0.CO;2](https://doi.org/10.1175/1520-0450(1992)031<1275:STCLDF>2.0.CO;2)
- Shupe, M. D., Intrieri, J.M., 2004. Cloud radiative forcing of the arctic surface: The influence of cloud properties, surface albedo, and solar zenith angle. *J. Clim.* 17, 616–628, [https://doi.org/10.1175/1520-0442\(2004\)017<0616:CRFOTA>2.0.CO;2](https://doi.org/10.1175/1520-0442(2004)017<0616:CRFOTA>2.0.CO;2)
- 1005 Sicard, M., Bertolín, S., Mallet, M., Dubuisson, P., Comerón, A., 2014. Estimation of mineral dust long-wave radiative forcing: sensitivity study to particle properties and application to real cases in the region of Barcelona. *Atmos. Chem. Phys.* 14. <https://doi.org/10.5194/acp-14-9213-2014>.
- Sorribas, M., Adame, J.A., Andrews, E., Yela, M., 2017. An anomalous African dust event and its impact on aerosol radiative forcing on the Southwest Atlantic coast of Europe in February 2016. *Sci.Tot. Environ.* 583, 269–279. <https://doi.org/10.1016/j.scitotenv.2017.01.064>.
- 1010 Stubenrauch, C.J., Rossow, W.B., Kinne, S., Ackerman, S., Cesana, G., Chepfer, H., DiGirolamo, L., Getzewich, B., Guignard, A., Heidinger, A., Maddux, B.C., Menzel, W.P, Minnis, P., Pearl, C., Platnick, S., Poulsen, C., Riedi, J., Sun-Mack, S., Walther, A., Winker, D., Zeng, S., and Zhao, G., 2013. Assessment of global cloud datasets from satellites: Project and database initiated by the

- 1015 GEWEX radiation panel. *Bull. Am. Meteorol. Soc.* 94(7), 1031-1049. <https://doi.org/10.1175/BAMS-D-12-00117.1>.
- Toledano, C., Cachorro, V.E., De Frutos, A.M., Sorribas, M., Prats, N., De la Morena, B.A., 2007. Inventory of African desert dust events over the southwestern Iberian Peninsula in 2000–2005 with an AERONET Cimel Sun photometer. *J. Geophys. Res. Atmos.* 112 (D21). <https://doi.org/10.1029/2006JD008307>.
- 1020 Turner, J., Parisi, A.V., 2018. Ultraviolet Radiation Albedo and Reflectance in Review: The Influence to Ultraviolet Exposure in Occupational Settings. *Int. J. Environ. Res. Public H.*, 15, 1507. <https://doi.org/10.3390/ijerph15071507>.
- Ullrich, R., Hoose, C., Möhler, O., Niemand, M., Wagner, R., Höhler, K., Hiranuma, N., Saathoff, H., Leisner, T., 2017. A New Ice Nucleation Active Site Parameterization for Desert Dust and Soot. *J. Atmos. Sci.*, 74, 699-717. <https://doi.org/10.1175/JAS-D-16-0074.1>.
- 1025 Valenzuela, A., Costa, M.J., Guerrero-Rascado, J.L., Bortoli, D., Olmo, F.J., 2017. Solar and thermal radiative effects during the 2011 extreme desert dust episode over Portugal. *Atmos. Environ.* 148, 16-29. <https://doi.org/10.1016/j.atmosenv.2016.10.037>.
- Vilaplana, J.M., Serrano, A., Antón, M., Cancillo M.L., Parias, M., Gröbner, J., Hülsen, G., Zablocky, G., Díaz, A., de la Morena, B., 2009. Report of the “El Arenosillo”/INTA-COST Calibration and Intercomparison campaign of UVER broadband radiometers. COST Action 726. ISBN: 978-84-692-2640-7, COST Office, pp. 64.
- 1030 Wacker, S., Grobner, J., Nowak, D., Vuilleumier, L. and Kampf, N., 2011. Cloud effect of persistent stratus nebulosus at the Payerne BSRN site. *Atmos. Res.* 102, 1[1]9. <https://doi.org/10.1016/j.atmosres.2011.06.007>.
- Welton, E.J., Campbell, J.R., Spinhirne, J.D., Scott III, V.S., 2001. Global monitoring of clouds and aerosols using a network of micropulse lidar systems, in: *Lidar Remote Sensing for Industry and Environment Monitoring* (Eds). International Society for Optics and Photonics. Vol. 4153, pp. 151-158.
- 1040 Winker, D.M., Vaughan, M.A., Omar, A., Hu, Y., Powell, K. A., Liu, Z., Hunt, W.H., Young, S.A., 2009. Overview of the CALIPSO mission and CALIOP data processing algorithms. *J. Atmos. Ocean. Tech.* 26 (11), 2310-2323. <https://doi.org/10.1175/2009JTECHA1281.1>.
- Young, S.A., 1995. Analysis of lidar backscatter profiles in optically thin clouds, *Appl. Optics* 34, 7019–7031. <http://dx.doi.org/10.1364/AO.34.007019>.
- 1045

Table captions

1050 **Table 1.** Both the height (z^{tropo} , km) and temperature (T^{tropo} , °C) of the tropopause and the altitude at which the temperature threshold of -37°C is reached (z^{-37} , in km), as obtained from GDAS temperature profiles.

Table 2. AERONET daily-averaged AOD at 500 nm together with the SSA (ω_0) and asymmetry parameter (g) values used in RT simulations for each day.

1055 **Table 3.** Mean optical and geometrical properties for the COD-predominant Ci group (N denotes the number of profiles examined for each Ci type). τ_{cc} , S_{cc} , z_{top} , z_{base} , Δz , T_{top} and T_{base} stand for, respectively, the COD, the LR, both the cloud top and base height boundaries, the geometrical thickness, and both the temperatures at z_{top} and z_{base} . T_m is the representative temperature of the Ci clouds (see **Eq. (12)**). Their mean effective radius, R_{eff} (in μm), and also the generalised effective size, D_{ge} , and Ice Water Path, IWP (in g m^{-2}), are also included. Note that
1060 the opCi category is also detached into two sub-groups, opCi-1 and opCi-2.

Table 4. Mean $CCRE$ values (W m^{-2}) at TOA and SRF, and the atmospheric $CCRE$, as obtained within the overall SW interval and the single UV, VIS and NIR bands, for the COD-predominant Ci group (their mean τ_{cc} is in parenthesis, see **Table 3**). Linear regression parameters for all the Ci cases observed at day-times (N=35) describing the Ci cooling effect, i.e., both the negative
1065 increasing rate (ν , $\text{W m}^{-2}\tau^{-1}$) and the correlation coefficient (r), are also included.

Figure captions

1070

Figure 1. The environment of El Arenosillo station (ARN/Huelva), located at the Southwest Iberian Peninsula (37.1° N 6.7° W, 40 m a.s.l.). Both the radiation instrumentation and the lidar system are also marked in red, separated around 100 m distance.

1075

Figure 2. Cirrus (Ci) clouds observed on: (a) 01 October 2016, (b) 08 May 2017, and (c) 28 October 2016 at the El Arenosillo station (ARN/Huelva). (Top panels) Contour plots of the vertical normalized backscattering ratio (R_{norm}) along the day; the predominant COD-type Ci clouds are also marked by coloured time intervals: svCi in red, stCi in green, and opCi in blue, and the particular profiles shown in the bottom panels are also indicated (by coloured dashed arrows). (Bottom panels) Those selected (in top panels) profiles of the extinction coefficient (σ_c , km⁻¹) and the corresponding linear volume depolarization ratio (δ^V). Their lidar-derived COD (τ_{cc}) and LR (S_{cc}) values are also included in the legend.

1080

1085

Figure 3. Images obtained with an all-sky camera at those times coincident with the detection of Ci clouds on: (Left) 01 October 2016 (svCi), (Centre) 08 May 2017 (stCi), and (Right) 28 October 2016 (opCi). For instance, times shown in each image correspond to the Ci profiles shown in **Fig. 2**.

1090

Figure 4. (Top panels, a-d) SW solar global radiation (SGR) levels measured on surface at El Arenosillo/Huelva station (full circles, and their error bars) and their corresponding RT simulations (no-Ci mode) (open circles) as a function of the Solar Zenith Angle (SZA): (a) during a mostly cloud-free and clean day on 15 October 2016 (black), and the three selected days with predominant COD-type Ci detection: (b) 01 October 2016 (svCi) (red), (c) 08 May 2017 (stCi) (green), and (d) 28 October 2016 (opCi) (blue), where the Ci features were removed; and (e) linear regression analysis of the SW SGR between simulations (SGR_s) and measurements (SGR_m), where the correlation coefficient, r , is shown within the legend for each day (N denotes the number of points used; coloured symbols correspond to those same as shown in the previous panels; and 1:1 line is also marked in black). (Bottom panels, a-d) SGR differences ($W\ m^{-2}$), $\Delta = SGR_s - SGR_m$ (full triangles) for those same days as shown in the top panels.

1095

1100

Figure 5. SW CCRE values ($W\ m^{-2}$) as estimated for the selected Ci cases as a function of the SZA at: (a) the top-of-atmosphere (TOA), $CCRE_{SW}^{TOA}$ (circles), and (b) on the surface (SRF), $CCRE_{SW}^{SRF}$ (triangles), together with (c) the atmospheric CCRE, $CCRE_{SW}^{atm}$ (squares), and (d) their corresponding IWP ($g\ m^{-2}$) (stars) for the three COD-type Ci clouds: svCi (red), stCi (green), and opCi (blue) cases. Note that the opCi category is also detached into two sub-groups, opCi-1 (cyan) and opCi-2 (dark blue), in dependence on their particular τ_{cc} range: 0.3-0.7 and 0.7-3.0, respectively.

1105

Figure 6. (Top) SW CCRE values ($W\ m^{-2}$) as obtained at TOA (red) and SRF (green), and the atmospheric CCRE (blue) for all the Ci cases in dependence with their particular COD (the corresponding values within the UV, VIS and NIR bands are shown in **Table 4**). Dashed lines represent the linear regression fitting performed for those three CCRE. (Bottom) the ice water path, IWP ($g\ m^{-2}$) (full stars) and the effective radius, R_{eff} (μm) (open stars), for all the same Ci cases within each Ci category: svCi, stCi, and opCi.

1110